

Neutron Scattering study of $\text{Sr}_2\text{Cu}_3\text{O}_4\text{Cl}_2$

Y. J. Kim^a

*Division of Engineering and Applied Sciences, Harvard University, Cambridge, Massachusetts 02138
and Center for Materials Science and Engineering,
Massachusetts Institute of Technology, Cambridge, Massachusetts 02139*

R. J. Birgeneau,^b F. C. Chou, M. Greven,^c M. A. Kastner, Y. S. Lee,^d and B. O. Wells^e

Center for Materials Science and Engineering, Massachusetts Institute of Technology, Cambridge, Massachusetts 02139

A. Aharony, O. Entin-Wohlman, and I. Ya. Korenblit

School of Physics and Astronomy, Tel Aviv University, Tel Aviv 69978, Israel

A. B. Harris

Department of Physics, University of Pennsylvania, Philadelphia, Pennsylvania 19104

R. W. Erwin

Center for Neutron Research, National Institute of Standards and Technology, Gaithersburg, Maryland 20899

G. Shirane

Department of Physics, Brookhaven National Laboratory, Upton, New York 11973

(Dated: November 19, 2018)

We report a neutron scattering study on the tetragonal compound $\text{Sr}_2\text{Cu}_3\text{O}_4\text{Cl}_2$, which has two-dimensional (2D) interpenetrating Cu_I and Cu_{II} subsystems, each forming a $S = 1/2$ square lattice quantum Heisenberg antiferromagnet (SLQHA). The mean-field ground state is degenerate, since the inter-subsystem interactions are geometrically frustrated. Magnetic neutron scattering experiments show that quantum fluctuations lift the degeneracy and cause a 2D Ising ordering of the Cu_{II} subsystem. Due to quantum fluctuations a dramatic increase of the Cu_I out-of-plane spin-wave gap is also observed. The temperature dependence and the dispersion of the spin-wave energy are quantitatively explained by spin-wave calculations which include quantum fluctuations explicitly. The values for the nearest-neighbor superexchange interactions between the Cu_I and Cu_{II} ions and between the Cu_{II} ions are determined experimentally to be $J_{I-II} = -10(2)\text{meV}$ and $J_{II} = 10.5(5)\text{meV}$, respectively. Due to its small exchange interaction, J_{II} , the 2D dispersion of the Cu_{II} SLQHA can be measured over the whole Brillouin zone with thermal neutrons, and a novel dispersion at the zone boundary, predicted by theory, is confirmed. The instantaneous magnetic correlation length of the Cu_{II} SLQHA is obtained up to a very high temperature, $T/J_{II} \approx 0.75$. This result is compared with several theoretical predictions as well as recent experiments on the $S = 1/2$ SLQHA.

I. INTRODUCTION

Quantum magnetism has been studied for many decades since the advent of quantum mechanics. Most of the early theoretical work is based on semi-classical methods such as spin-wave theory. Quite remarkably, spin-wave theory has been successful in describing many physical properties of a variety of magnetic systems. Despite the fact that it is essentially a $1/(zS)$ expansion,¹ where z is the coordination number, and thus one would

expect it to be less accurate for a small spin quantum number S , spin-wave theory has been a very powerful tool in investigating quantum magnetism, and the “semi-classical” description of quantum magnets has been sufficient to understand most experimental results. In a seminal paper, Haldane pointed out the special significance of the spin quantum number in one-dimensional (1D) quantum Heisenberg antiferromagnet (QHA).² In his now famous conjecture, he mapped the 1D QHA onto the quantum nonlinear σ model (QNL σ M), and noted the

fundamental difference in the ground states for half-odd-integer S and integer S . Specifically, the 1D QHA with half-odd-integer S has a quasi-long-range ordered ground state with a gapless excitation spectrum, while that with integer S has a quantum disordered ground state with a large energy gap in the excitation spectrum. Subsequent developments of quantum field theory, numerical simulations and experiments have confirmed Haldane's conjecture.

In contrast, quantum effects in the two-dimensional (2D) QHA are typically less dramatic. In fact, the qualitative behavior of the 2D QHA is similar to that of the classical one.³ Quantum fluctuations usually manifest themselves through uniform renormalization of physical quantities, such as the staggered magnetization or the spin-wave velocity. However, in certain magnetic systems, where the primary exchange couplings are highly frustrated, the effects of quantum fluctuation can be revealed *qualitatively* in the low-energy spin dynamics. As an example, isostructural compounds $\text{Sr}_2\text{Cu}_3\text{O}_4\text{Cl}_2$ and $\text{Ba}_2\text{Cu}_3\text{O}_4\text{Cl}_2$, the so-called 2342 materials, offer a dramatic and clear demonstration of such quantum effects as "order from disorder".⁴ In this paper, we describe our detailed neutron scattering study of the frustrated 2D $S = 1/2$ antiferromagnet $\text{Sr}_2\text{Cu}_3\text{O}_4\text{Cl}_2$, including experimental evidence for quantum fluctuation induced order. Some of the results reported here were briefly presented in a recent letter.⁵

The discovery of high temperature superconductivity in 1986 has triggered much work on the magnetism in lamellar copper oxides. These materials contain CuO_2 planes whose 2D spin fluctuations can be modeled by the $S = 1/2$ square lattice (SL) QHA. Through a combination of experimental, numerical, and theoretical efforts, a quantitative understanding of the $S = 1/2$ SLQHA has emerged.^{3,6,7,8} Notably, neutron scattering measurements of the instantaneous spin-spin correlation length of the model compound $\text{Sr}_2\text{CuO}_2\text{Cl}_2$ are found to be in quantitative agreement with quantum Monte Carlo results and both in turn are well-described by analytic theory for the QNL σ M.⁷ Angle resolved photoemission spectroscopy (ARPES) on this insulating system has also provided important information on the behavior of a single hole in a paramagnetic background, hence testing the applicability of the $t - J$ model.^{9,10}

The structure of $\text{Sr}_2\text{Cu}_3\text{O}_4\text{Cl}_2$, shown in Fig. 1(a), is similar to that of $\text{Sr}_2\text{CuO}_2\text{Cl}_2$. As shown in Fig. 1(b), the CuO_2 layers are replaced by Cu_3O_4 layers, which contain an additional Cu_{II}^{2+} ion at the center of every second plaquette of the original Cu_IO_2 square lattice.^{11,12} The configuration in the neighboring plane is obtained by translating the whole plane by $(\frac{a}{2}, \frac{a}{2})$. The in-plane isotropic interaction J_{I-II} between Cu_I and Cu_{II} subsystems is frustrated such that they form interpenetrating $S = 1/2$ SLQHA's with respective exchange interactions J_I and J_{II} .

Due to the *complete* frustration of the isotropic coupling between Cu_I and Cu_{II} , 2342 exhibits many fasci-

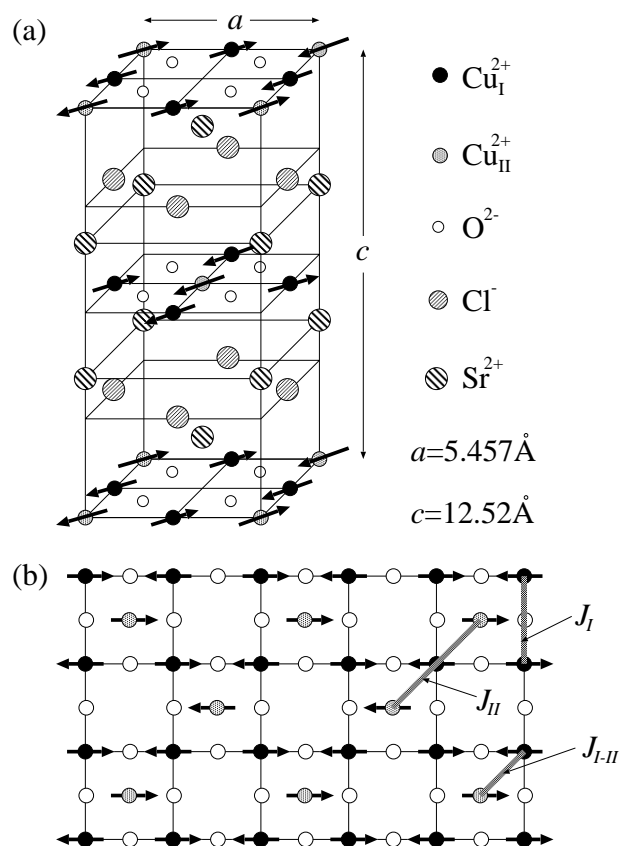


FIG. 1: (a) Crystal and magnetic structure of $\text{Sr}_2\text{Cu}_3\text{O}_4\text{Cl}_2$. Ordered spin directions for copper spins are shown as arrows. (b) Cu_3O_4 plane and various exchange interactions between spins.

ating magnetic phenomena. In their magnetic susceptibility and electron paramagnetic resonance measurements on $\text{Ba}_2\text{Cu}_3\text{O}_4\text{Cl}_2$ powder, Noro and coworkers¹³ first observed anomalous features at $T \sim 320\text{K}$ and $T \sim 40\text{K}$ and attributed these to respective antiferromagnetic ordering of the Cu_I and Cu_{II} spins. Subsequent neutron scattering measurements by Yamada *et al.*¹⁴ showed that 2342 exhibits antiferromagnetic order of the Cu_I and Cu_{II} subsystems below the respective Néel temperatures $T_{N,I}$ and $T_{N,II}$. Far-infrared electron spin resonance (ESR)¹⁵ and submillimeter wave resonance experiments¹⁶ showed that there is a low energy out-of-plane excitation in the long-wavelength limit. The dispersion of a single hole in both antiferromagnetic and paramagnetic spin background was measured simultaneously in the same Cu_3O_4 plane by ARPES experiments on 2342.^{17,18,19} One of the most intriguing features in earlier studies is the weak ferromagnetic moment that appears below $T_{N,I}$.^{13,14,20,21} We have recently reported that anisotropic bond-dependent interactions such as pseudo-dipolar couplings can in fact explain such weak ferromagnetic moments.^{20,22}

We consider two specific consequences of the frustration in this paper. First, in the mean field approximation, the Cu_I and Cu_{II} subsystems are decoupled, so that in addition to the well known Cu_I SLQHA, the Cu_{II} 's form their own $S = 1/2$ SLQHA with an order of magnitude smaller superexchange, J_{II} . Chou *et al.*²⁰ have shown that the magnetic susceptibility of the Cu_{II} subsystem is very well described as a $S = 1/2$ SLQHA by comparing the experimental result with the results of a quantum Monte Carlo calculation. Since $J_{II} \sim 10$ meV is matched well with the energy of thermal neutrons, this is an ideal $S = 1/2$ SLQHA system for neutron scattering experiments. In Sec. IV D, we show the spin-wave dispersion of the Cu_{II} subsystem throughout the entire Brillouin zone, including a theoretically predicted dispersion along the zone boundary. In Sec. V B, the correlation length data measured from the Cu_{II} SLQHA are presented as a function of temperature and compared with various theoretical predictions as well as quantum Monte Carlo results. Because J_{II} is an order of magnitude smaller than J_I , we are able to access a rather high temperature ($T/J_{II} \approx 0.75$).

Second, because of the frustration, we can observe the direct effect of quantum fluctuations. When a system can be separated into two Heisenberg antiferromagnetic sublattices, so that the molecular field of the spins in each sublattice vanishes on the spins of the other, then within mean field theory the ground state has a degeneracy with respect to the relative orientation of the sublattices, and the excitation spectrum contains two distinct sets of zero energy (Goldstone) modes, reflecting the fact that these subsystems can be rotated independently without cost in energy. This degeneracy is removed by fluctuations. Shender⁴ showed that quantum spin-wave interactions prefer collinearity of the spins in the two sublattices. This has the following experimental consequences in $\text{Sr}_2\text{Cu}_3\text{O}_4\text{Cl}_2$: The symmetry of the critical fluctuations of the Cu_{II} system is lowered to Ising due to the fluctuation-driven collinearity, and the spin-wave mode corresponding to the relative rotation of sublattice moments develops a gap. Indeed, such a gap was considered in the garnet $\text{Fe}_2\text{Ca}_3(\text{GeO}_4)_3$. However, since a similar gap could also arise from crystalline magnetic anisotropy, the final identification was rather complex.^{23,24,25}

Our inelastic neutron data in Sec. IV show a dramatic increase of the Cu_I “out-of-plane” gap below $T_{N,II}$ (see Fig. 9), which clearly reflects a coupling between the Cu_I and Cu_{II} spins. However, within mean field theory this coupling due to frustrated interactions must vanish by symmetry. Accordingly, we conclude that the enhanced gap for $T < T_{N,II}$ is due to *quantum fluctuations*. Heuristically, the lowering of the symmetry on the Cu_{II} site due to the ordering of the Cu_I 's is sensed through the quantum fluctuations. This identification is corroborated further by detailed theoretical calculations, which use parameters determined independently, albeit less accurately, by the susceptibility measurements.²⁰

There have been numerous studies on this peculiar *or-*

der from disorder effect on various systems. Villain *et al.*²⁶ studied a generalized frustrated Ising model in two dimensions and found that the system does not have long range order at $T = 0$, but is ferromagnetically ordered at low but non-zero temperature; *thermal fluctuations* are necessary to stabilize the ordered state; thus they termed this phenomenon *order from disorder*. Shender⁴ showed that *quantum fluctuations* can also cause order from disorder phenomena in frustrated magnetic systems. In addition to thermal or quantum disorder, substitutional disorder also causes ordering in such frustrated magnetic systems. Henley²⁷ studied order from substitutional disorder in a planar antiferromagnet on a square-lattice with a strong second nearest neighbor exchange and discovered that anti-collinear order is stabilized by substitutional disorder, in contrast with the collinear ground state due to thermal or quantum disorder. Chandra *et al.*²⁸ investigated the Heisenberg model on such a lattice using analogies between quantum antiferromagnetism and superfluidity. The Heisenberg antiferromagnet on the layered body centered tetragonal structure, where the inter-planar coupling is fully frustrated, has been also studied extensively, mainly due to its similarity to the structure of high temperature superconductors.^{29,30,31,32}

The result of our neutron scattering measurements on single crystals of $\text{Sr}_2\text{Cu}_3\text{O}_4\text{Cl}_2$ are presented in the following sections. In Sec. II, a brief description of magnetic neutron scattering is given. In Sec. III A, our elastic neutron scattering results along with the spin structure deduced from these results are presented. The order parameter measurements for both the Cu_I ordering and the Cu_{II} ordering are shown in Sec. III B. The spin-wave calculations as well as our inelastic neutron scattering results are discussed in Sec. IV. Section IV contains a large amount of data; therefore, it is divided into four subsections. We briefly discuss the theoretical spin-wave calculation in Sec. IV A. Spin-waves at $T > T_{N,II}$, where the Cu_I - Cu_{II} interaction can be ignored, are presented in Sec. IV B. The Cu_I - Cu_{II} interaction at $T < T_{N,II}$ and the effect of quantum fluctuations on the spin dynamics are discussed in Sec. IV C. In Sec. IV D, the 2D dispersion of the $S = 1/2$ SLQHA (Cu_{II} subsystem) is presented. We have also studied the critical behavior of the $S = 1/2$ SLQHA by measuring the static correlation length, which is presented in Sec. V. Finally, some unresolved issues and future experiments are discussed in Sec. VI.

II. MAGNETIC NEUTRON SCATTERING

A General cross section

In a neutron scattering experiment, the key variables are the neutron energy change and the concomitant change in neutron wave vector. We denote the momen-

tum and energy transfer by \mathbf{Q} and ω , which are given by $\mathbf{Q} \equiv \mathbf{k}_i - \mathbf{k}_f$ and $\omega \equiv E_i - E_f$, respectively. We use units in which $\hbar = k_B = 1$ and the scattering vector $\mathbf{Q} = (\frac{2\pi}{a}H, \frac{2\pi}{a}K, \frac{2\pi}{c}L)$. Throughout this paper, we use \mathbf{q} to denote physically relevant momentum transfer; that is, the momentum transfer with respect to the reciprocal lattice vector \mathbf{G} : $\mathbf{q} \equiv \mathbf{Q} - \mathbf{G}$.

The partial differential cross section for spin only scattering of unpolarized neutrons is given by^{33,34}

$$\frac{d^2\sigma}{d\Omega dE_f} \sim \frac{k_f}{k_i} f^2(\mathbf{Q}) \sum_{\alpha\beta} (\delta_{\alpha\beta} - \hat{Q}_\alpha \hat{Q}_\beta) S^{\alpha\beta}(\mathbf{Q}, \omega), \quad (1)$$

where $\hat{\mathbf{Q}} \equiv \mathbf{Q}/Q$, and $f(\mathbf{Q})$ is the magnetic form factor, which is the Fourier transform of the spin-density distribution around the magnetic ion, and hence depends on \mathbf{Q} .³⁵

An important feature of magnetic scattering is the directional dependence through the *geometric factor* $(\delta_{\alpha\beta} - \hat{Q}_\alpha \hat{Q}_\beta)$, which picks out the components of the magnetization *perpendicular* to the momentum transfer \mathbf{Q} . The quantity $S^{\alpha\beta}(\mathbf{Q}, \omega)$, known as the *dynamic structure factor*, is the Fourier transform in both space and time of the spin-spin correlation function. The latter is the thermal average over the correlations between the component along the α -axis of a spin at the origin at time zero and the component along the β -axis of a spin at site \mathbf{r} at time t :

$$S^{\alpha\beta}(\mathbf{Q}, \omega) = \frac{1}{2\pi} \sum_{\mathbf{r}} \int_{-\infty}^{\infty} dt e^{i(\mathbf{Q}\cdot\mathbf{r} - \omega t)} \langle S^\alpha(\mathbf{0}, 0) S^\beta(\mathbf{r}, t) \rangle. \quad (2)$$

The *static structure factor* is obtained from the Fourier transformation of the *equal-time* correlation function, and measures the *instantaneous* correlations between the spins:

$$S^{\alpha\beta}(\mathbf{Q}) = \int_{-\infty}^{\infty} d\omega S^{\alpha\beta}(\mathbf{Q}, \omega). \quad (3)$$

In principle, one can obtain the static structure factor by directly measuring the entire dynamical spectrum $S(\mathbf{Q}, \omega)$ and doing the energy integration at each \mathbf{Q} . However, in most systems this is impossible within a reasonable time scale. Fortunately, in 2D magnetic systems such as the lamellar copper oxides, the energy integration is effectively done by detecting neutrons without energy discrimination in a special scattering geometry. One then can determine the instantaneous correlation function in one scan.³⁶

B Elastic scattering cross section

For elastic neutron scattering from collinearly ordered magnetic moments, the scattered intensity can be obtained from Eq. (1):

$$I(\mathbf{Q}) \sim f(\mathbf{Q})^2 (1 - (\hat{\mathbf{Q}} \cdot \hat{\mathbf{e}})^2) |F_M(\mathbf{Q})|^2, \quad (4)$$

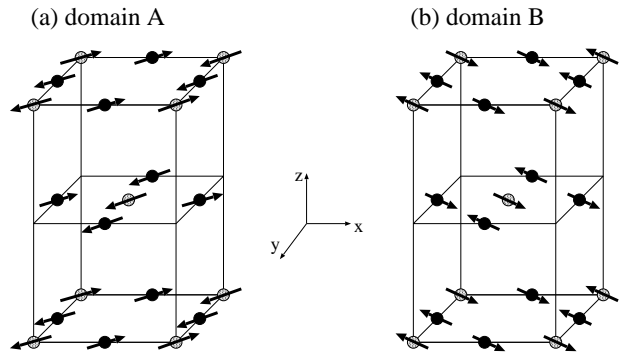


FIG. 2: Two magnetic domains present in $\text{Sr}_2\text{Cu}_3\text{O}_4\text{Cl}_2$ at zero magnetic field.

where $\hat{\mathbf{e}}$ the direction of the staggered magnetization. There are three factors contributing to the intensity of magnetic Bragg peaks: the geometric factor $(1 - (\hat{\mathbf{Q}} \cdot \hat{\mathbf{e}})^2)$, the magnetic structure factor $F_M(\mathbf{Q})$, and the magnetic form factor $f(\mathbf{Q})$.

We also need to consider magnetic domains due to the tetragonal symmetry of the crystal. Consider the two types of structure shown in Fig. 2, where only Cu spins are shown. In a realistic single crystal in zero magnetic field, these two types of magnetic domain can be equally populated. These two domains give rise to different magnetic reciprocal lattice vectors. As shown in Fig. 3, different domains give different Cu_{II} magnetic Bragg reflections, which will prove useful in elucidating the spin structure of the Cu_{II} magnetic lattice. The Cu_I magnetic peaks, on the other hand, only occur on top of allowed nuclear Bragg reflections, and do not occur in the $(H K 0)$ zone.

C Inelastic scattering cross section

In conventional spin-wave theory for a two-sublattice antiferromagnet, one obtains two eigenmodes. If the spins are ordered in the z -direction, the two modes have eigenvectors in the direction of x and y . For a Heisenberg model, these two modes are gapless Goldstone modes due to the continuous symmetry. However, in the presence of an uniaxial anisotropy, this continuous symmetry is broken, and both modes obtain energy gaps; this energy gap corresponds to the energy cost in rotating the spins away from the z -direction. For an XY anisotropy, only one mode has an energy gap, corresponding to the energy cost in rotating spins out of the xy -plane. The other mode is a zero-energy mode at $\mathbf{q}=0$, since the continuous symmetry is preserved in the xy -plane. Since the polarization of the eigenvector of the gapped mode is perpendicular to the xy -plane, we call this mode an out-of-plane mode, while the gapless mode is called an in-plane mode.

The direction of the eigenvectors plays an important

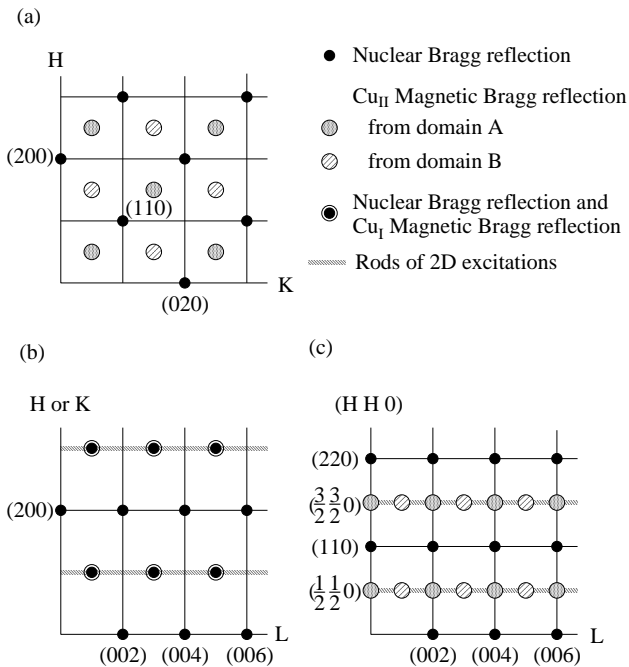


FIG. 3: Reciprocal lattice diagrams of the three different 2D zones employed in our experiment: (a) $(H K 0)$ zone, (b) $(H 0 L)$ zone, or equivalently, $(0 K L)$ zone, and (c) $(H H L)$ zone. Note that Cu_I magnetic Bragg reflections coincide with nuclear Bragg positions.

role in the neutron scattering cross section. By considering geometric factors for both domains in Fig. 2, one can show that the inelastic cross section from spin-waves reduces to

$$\frac{d^2\sigma}{d\Omega dE_f} \sim f^2(\mathbf{Q}) \frac{k_f}{k_i} \left[\frac{1 + \cos^2\phi}{2} S^{\parallel}(\mathbf{Q}, \omega) + \sin^2\phi S^{\perp}(\mathbf{Q}, \omega) \right], \quad (5)$$

where ϕ is the angle subtended by \mathbf{Q} and $[0 0 1]$, and S^{\parallel} and S^{\perp} denote the dynamic structure factor of the in-plane and out-of-plane spin-wave modes, respectively. The out-of-plane component of the dynamic structure factor, $S^{\perp}(\mathbf{Q}, \omega)$, is well approximated by

$$S^{\perp}(\mathbf{Q}, \omega) = \frac{1}{\omega_{\perp}} \left[\frac{1 + n(\omega_{\perp})}{\Gamma^2 + (\omega_{\perp} - \omega)^2} + \frac{n(\omega_{\perp})}{\Gamma^2 + (\omega_{\perp} + \omega)^2} \right], \quad (6)$$

where $n(\omega_{\perp}) = 1/(e^{\omega_{\perp}/T} - 1)$ is the Bose population factor, Γ^{-1} is a small magnon lifetime, and ω_{\perp} is the out-of-plane gap. A similar relation holds for the in-plane component $S^{\parallel}(\mathbf{Q}, \omega)$ with ω_{\parallel} replacing ω_{\perp} .

D Experimental details

We have carried out both inelastic and elastic neutron scattering experiments with the triple-axis spectrometers

at the High Flux Beam Reactor (HFBR), Brookhaven National Laboratory, and at the National Institute of Standards and Technology, Center for Neutron Research (NCNR). Our measurements were done mostly on thermal beamlines at these facilities, except for the data shown in Fig. 12, which were obtained using cold neutrons. Large (dimension $2 \times 2 \times 0.5 \text{ cm}^3$) single crystals of $\text{Sr}_2\text{Cu}_3\text{O}_4\text{Cl}_2$, grown by slow cooling of a melt containing a CuO flux, are used in the experiment. The crystals remain tetragonal (space group $I4/mmm$) for $15\text{K} < T < 550\text{K}$ with lattice constants $a = 5.457\text{\AA}$ and $c = 12.52\text{\AA}$ at $T < 50\text{K}$.²²

The (002) reflection of pyrolytic graphite (PG) was used as both monochromator and analyzer. A PG filter was placed either before or after the sample to eliminate higher order contamination. Various experimental configurations with different sets of collimations and neutron energy were used. A typical setup used in the inelastic experiments was a fixed final neutron energy of $E_f = 14.7 \text{ meV}$ and collimations of 40° - 40° -Sample- 40° - 80° . The sample was sealed in an aluminum can filled with helium exchange gas, and mounted in a closed-cycle helium refrigerator. The temperature was controlled within $\pm 0.2\text{K}$ in the range $10\text{K} < T < 400\text{K}$.

III. ANTIFERROMAGNETIC ORDERING OF COPPER SPINS

Since the 2D SLQHA does not have long-range order at $T > 0$, such order must arise from spin anisotropy terms or inter-plane coupling. For $\text{Sr}_2\text{CuO}_2\text{Cl}_2$, as the Néel temperature is approached from above, successive crossovers from 2D Heisenberg to 2D XY to three-dimensional (3D) XY behavior are expected to take place, albeit with a 3D critical regime that is extremely narrow.^{7,37} For $\text{Sr}_2\text{Cu}_3\text{O}_4\text{Cl}_2$, on the other hand, the inter-plane coupling between Cu_I spins, $J_{I,3D}$, is larger than the XY anisotropy. Upon lowering the temperature in the paramagnetic phase, we then expect a crossover from 2D Heisenberg behavior, characterized by a spin-spin correlation length $\xi_0(T)$ that increases exponentially in T^{-1} , to 3D Heisenberg behavior at a temperature given by the relation $\xi_0^2 J_{I,3D}/J_I \sim 1$, where $J_{I,3D}$ is the interplane coupling between Cu_I spins.³⁸ In other words, we expect 3D effects to become important for $\xi_0/a \sim 30$. The correlation length of the SLQHA is known to be about 40 lattice constants at $T/J \simeq 0.26$.^{6,39} For $J_I \simeq 130 \text{ meV}$, this corresponds to a temperature of $\sim 390\text{K}$, which agrees with $T_{N,I}$.

Unlike for the Cu_I subsystem, the isotropic inter-plane Cu_{II} - Cu_{II} coupling is frustrated, similar to that of $\text{Sr}_2\text{CuO}_2\text{Cl}_2$;⁷ therefore, $T_{N,II}$ is expected to be determined mostly by spin anisotropies, originating from both in-plane quantum fluctuations and from inter-plane dipolar and pseudodipolar interactions. For $T < T_{N,I}$, the ordered Cu_I spins fluctuate mainly in the directions

transverse to their staggered moment $\mathbf{M}_{s,I}$. J_{I-II} then generates fluctuations in the Cu_{II} spins along the same direction, causing an effective reduction in the corresponding transverse exchange components of J_{II} .⁴ This yields an effective biquadratic term $-\tilde{\delta}(\mathbf{S}_I \cdot \mathbf{S}_{II})^2$, where $\tilde{\delta} \propto J_{I-II}^2/(J_I + J_{II})$. This implies an effective Ising-like anisotropy $J_{II}\alpha_{II}^{eff} \propto \tilde{\delta}\mathbf{S}_I^2$, which favors ordering of the Cu_{II} spins collinearly with \mathbf{S}_I , consistent with our measured structure, Fig. 1(a). Indeed, $T_{N,II} \sim 40\text{K}$ agrees with $\xi_0(T_{N,II})^2\alpha_{II}^{eff} \sim 1$, where $\alpha_{II}^{eff} \sim 0.01$ is independently deduced from our spin-wave gaps, as discussed in Sec. IV D. We next show experimentally that the ordering direction of Cu_{II} spins is indeed parallel to that of the Cu_I subsystem, and that this ordering is a 2D Ising transition.

A Magnetic structure

The Cu_I spin ordering direction shown in Fig. 1 has been determined in previous magnetization measurements.²² This ordering is similar to that in a bilayer cuprate $\text{YBa}_2\text{Cu}_3\text{O}_6$. Unlike other “214” type materials, the Cu_I spins of “2342” have unique nearest neighbors in the c -direction, just like $\text{YBa}_2\text{Cu}_3\text{O}_6$. For such a structure, the observed ordering direction along the Cu-O-Cu bonds has been attributed to the quantum fluctuations.⁴⁰

Next, let us consider Cu_{II} magnetic diffraction peaks in the $(H K 0)$ zone. In Table I, we summarize our results. The neutron energy was fixed at 14.7 meV, and collimations of $20^\circ\text{-}40^\circ\text{-S-}40^\circ\text{-}80^\circ$ were used. One can fit the peak intensities with Eq. (4) with $\hat{\mathbf{e}}$ as a free parameter. The fit gives the spin direction shown in Fig. 2; namely, $\hat{\mathbf{e}}$ along the $[1 \bar{1} 0]$ direction for domain A, and along the $[1 1 0]$ direction for domain B. In order to determine how the copper oxide layers are stacked, we show in Fig. 4 the peak intensity for each magnetic Bragg peak in the $(H H L)$ zone. From the domain structure and the stacking scheme in Fig. 2, one can show that magnetic Bragg peaks occur at even L due to domain A, together with magnetic Bragg peaks at odd L due to domain B. Since our momentum transfer, \mathbf{Q} , is along the $[H H L]$ direction, \mathbf{Q} is always perpendicular to the spin ordering direction, $\hat{\mathbf{e}}$, in domain A. However, in domain B, this is not true, and $\hat{\mathbf{e}} \cdot \hat{\mathbf{Q}} = \sin\phi$. Therefore, the geometric factor only matters for the peaks from domain B. As shown in Fig. 4, only the odd- L data exhibit the expected geometric factor dependence. In fact, the agreement is excellent between odd- L data (triangles) and the calculation (\times). It should be noted that the stacking scheme of the Cu_{II} spins is identical to that of $\text{Sr}_2\text{CuO}_2\text{Cl}_2$.⁴¹

In their study on $\text{YBa}_2\text{Cu}_3\text{O}_{6.15}$, Shamoto *et al.*⁴² reported an anisotropic Cu magnetic form factor, which depends not only on the magnitude of \mathbf{Q} , but also on the direction of \mathbf{Q} . Specifically, the magnetic form factor was found to drop more rapidly with increasing Q , if \mathbf{Q}

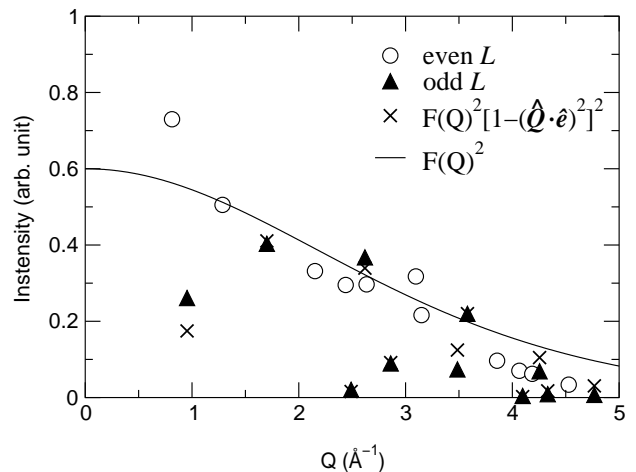


FIG. 4: Cu_{II} magnetic Bragg peak intensity for $(H H L)$ is plotted for even- L (open circle) and odd- L (closed triangle). The solid line is a plot of magnetic form factor of free Cu^{2+} ions.³⁵ The symbol \times represents the magnetic form factor squared multiplied by the geometric factor in Eq. (4). Clearly, even- L data show the same Q -dependence as the magnetic form factor, while odd- L data do not. The agreement between odd- L data and the calculated results are very good.

is perpendicular to the L -direction. The small deviation between the even- L data (open circles) and the solid line at large Q is probably due to this anisotropy in the magnetic form factor, since most of our large- Q data has a relatively small L -component.

From the magnetic Bragg peak intensity, we have also estimated the value of staggered magnetization at $T = 10\text{K}$ as $M_{s,I} \approx 0.4(2)\mu_B$ and $M_{s,II} \approx 0.8(2)\mu_B$ for Cu_I and Cu_{II} , respectively. Within experimental error bars these values reasonably agree with the theoretically expected value $0.6\mu_B$.⁴³

B Order parameters

The antiferromagnetic Bragg intensity is proportional to the square of the staggered magnetization, M_s , which is the order parameter of the Néel ordered phase. We measured the temperature dependence of the $(1 0 1)$ peak, using neutrons with energy 13.4meV and collimations of $20^\circ\text{-}40^\circ\text{-S-}40^\circ\text{-}80^\circ$. The temperature dependence of the magnetic Bragg intensity at the $(1 0 1)$ reciprocal lattice position is shown in Fig. 5(a). Since nuclear Bragg scattering is only weakly temperature dependent, we subtract the high-temperature $(1 0 1)$ nuclear intensity from the observed intensity. We also studied the temperature dependence of the $(3 0 1)$ peak, which shows the same temperature dependence as the $(1 0 1)$ peak.

We fit the $T > 300\text{K}$ data to the form $I \sim (T_N - T)^{2\beta}$,

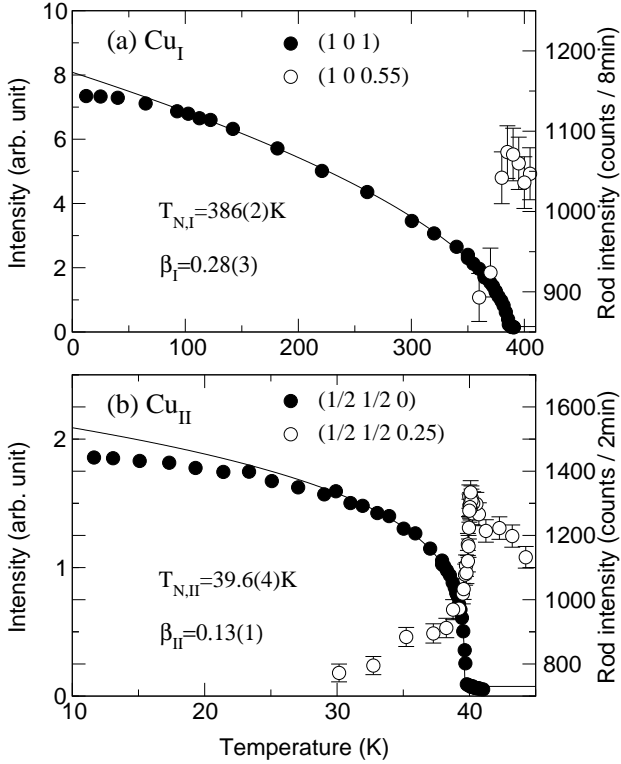


FIG. 5: (a) Filled circles are the integrated intensity of the 3D magnetic Bragg peak at (1 0 1). Open circles are the intensity on the 2D rod of Cu_I at (1 0 0.55). (b) The peak intensity of (1/2 1/2 0) peak is plotted as filled circles. Open circles are the intensity on the 2D rod of Cu_{II} at (1/2 1/2 0.25). Solid lines are fits to $\sim (T_N - T)^{2\beta}$ with the fitting parameters shown.

TABLE I: Cu_{II} magnetic Bragg intensity in (H K 0) zone at $T = 12\text{K}$. The observed intensity, $I(\text{obs})$, is neutron counts per minute. The intensity, $I(\text{cal})$, is calculated assuming the spin structure shown in Fig. 2. The crystallographic reliability index is $R = \sum \sqrt{I_{\text{obs}}} - \sqrt{I_{\text{cal}}} / \sum \sqrt{I_{\text{obs}}} = 0.12$.

H	K	Q (\AA^{-1})	domain	$I(\text{obs})$	$I(\text{cal})$
1/2	1/2	0.81	A	39163	40300
3/2	3/2	2.44	A	17073	9380
5/2	1/2	2.93	A	4041	4700
1/2	5/2	2.93	A	3744	4700
5/2	5/2	4.07	A	3679	3460
7/2	3/2	4.38	A	1637	2640
3/2	7/2	4.38	A	1848	2640
3/2	1/2	1.82	B	2736	3140
1/2	3/2	1.82	B	2542	3140
5/2	1/2	3.35	B	819	480
1/2	5/2	3.35	B	817	480
7/2	1/2	4.07	B	1162	1370
7/2	1/2	4.07	B	1035	1370

and obtained $T_{N,I} = 386(2)\text{K}$ and $\beta_I = 0.28(3)$; this result is plotted as a solid line in Fig. 5(a). β_I is consistent with that of La_2CuO_4 ,⁴⁴ while somewhat larger than that of $\text{Sr}_2\text{CuO}_2\text{Cl}_2$.⁷ We associate β_I with the 3D XY universality class, since the inter-plane coupling drives the 3D ordering in $\text{Sr}_2\text{Cu}_3\text{O}_4\text{Cl}_2$. On the other hand, the dominant spin anisotropy driving the ordering in $\text{Sr}_2\text{CuO}_2\text{Cl}_2$ is the XY anisotropy within the plane; thus the system is presumably closer to the 2D XY universality class at least not too near T_N .^{7,45} Ref. 45 also suggests that such XY systems might exhibit an order parameter exponent β close to $\frac{1}{4}$. Another possible explanation follows experiments on La_2CuO_4 , which were interpreted as being near a tricritical point, which would have exactly $\beta = \frac{1}{4}$.⁴⁶ However, it is not yet clear why many quasi-2D Heisenberg and XY systems happen to be near tricriticality.

For the Cu_{II} order parameter, we measure the intensity of the $(\frac{1}{2} \frac{1}{2} 0)$ reflection as a function of temperature. The neutron energy is fixed at 14.7 meV, and $10^\circ\text{-}40^\circ\text{-S-}40^\circ\text{-}80^\circ$ collimations are used. The peak intensities are shown in Fig. 5(b). As in the Cu_I case, the solid line is the result of fitting data for $T > 30\text{K}$ with $T_{N,II} = 39.6(4)\text{K}$ and $\beta_{II} = 0.13(1)$. This strongly suggests that the ordering of the Cu_{II} spins is in the 2D Ising universality class. As discussed in Sec. I, this provides strong evidence of fluctuation driven ordering. However, one cannot, from this measurement alone, rule out the possibility of the presence of crystalline Ising anisotropies in the $\text{Cu}_{II}\text{-Cu}_{II}$ superexchange interactions. As shown in Sec. IV, evidence from spin dynamics experiments is necessary to clarify this point.

Another way to probe the 3D magnetic ordering is to plot the intensity of the 2D magnetic rod as a function of temperature. Quasi-2D materials, such as K_2NiF_4 , La_2CuO_4 ,⁴⁷ and $\text{Sr}_2\text{CuO}_2\text{Cl}_2$,⁷ show strong 2D dynamic fluctuations above the 3D ordering temperature T_N ; this is exhibited as rods of scattering perpendicular to the 2D plane, whose locations are shown in Fig. 3. One can observe this by accepting all energies of neutrons at the detector in the two-axis configuration. At T_N , the 2D inelastic scattering intensity begins to decrease rapidly, as the spectral weight is shifted from 2D inelastic scattering to 3D Bragg scattering. Therefore, this measurement shows the 2D nature of the system, as well as the 3D transition temperature, complementing the order parameter measurement. In Fig. 5(a) and (b), we show these 2D rod intensities at (1 0 0.55) and at (0.5 0.5 0.25) for the Cu_I and Cu_{II} sublattices, respectively. Indeed, we see rapid decreases of both the Cu_I and the Cu_{II} 2D rod intensities as the system is cooled through their respective 3D Néel transitions. The non-zero intensity below the Néel temperature is due to the contributions from phonons.

TABLE II: Parameters used in the spin Hamiltonian [Eq. (7)]. These values are determined from our neutron scattering experiment. Superexchange energies are in units of meV and α is dimensionless.

	meaning	value
J_I	Cu _I -Cu _I superexchange (in-plane)	130(5)
J_{II}	Cu _{II} -Cu _{II} superexchange	10.5(5)
J_{I-II}	Cu _I -Cu _{II} superexchange	-10(2)
$J_{I,3D}$	Cu _I -Cu _I superexchange (out-of-plane)	0.14(2)
α_I	XY-anisotropy in J_I (T=200K)	$5.2(9) \times 10^{-4}$
α_{II}	XY-anisotropy in J_{II} (T=10K)	$1(5) \times 10^{-4}$

IV. SPIN DYNAMICS

The spin Hamiltonian used in the spin-wave calculation and the data analysis is as follows:

$$\mathcal{H} = \mathcal{H}_I + \mathcal{H}_{II} + \mathcal{H}_{int} \quad (7)$$

$$\mathcal{H}_I = J_I \sum_{\langle i,j \rangle_I} (\mathbf{S}_i \cdot \mathbf{S}_j - \alpha_I S_i^z S_j^z) + J_{I,3D} \sum_{\langle i,j \rangle_{I,3D}} \mathbf{S}_i \cdot \mathbf{S}_j$$

$$\mathcal{H}_{II} = J_{II} \sum_{\langle m,n \rangle_{II}} (\mathbf{S}_m \cdot \mathbf{S}_n - \alpha_{II} S_m^z S_n^z)$$

$$\mathcal{H}_{int} = J_{I-II} \sum_{\langle i,m \rangle_{I-II}} \mathbf{S}_i \cdot \mathbf{S}_m,$$

where i, j and m, n denote Cu_I sites and Cu_{II} sites, respectively. The symbols $\langle i, j \rangle_I$ and $\langle i, j \rangle_{I,3D}$ label Cu_I intra-planar and inter-planar nearest neighbors, whereas $\langle m, n \rangle_{II}$ and $\langle i, m \rangle_{I-II}$ refer to the nearest-neighbor Cu_{II}-Cu_{II} and Cu_I-Cu_{II} bonds, respectively. The reduced exchange anisotropy, $\alpha = (J - J^z)/J$, is used here, and is therefore dimensionless. We left out other smaller terms, such as the in-plane anisotropy in J_I and J_{II} , the pseudo-dipolar interaction between Cu_I and Cu_{II}, J_{pd} , the interplanar dipolar Cu_{II}-Cu_{II} interaction, and the four-fold anisotropy term.^{20,22} It turns out that these small terms do not affect the spin dynamics on the energy scale probed by thermal neutrons, although they are essential in explaining such behavior as the spin-flop transition or ESR experiment results.^{20,22,48} The parameters

$$\omega_1 = S \sqrt{32J_{II}\delta x_3 / (\delta + 2x_3)} \quad (8)$$

$$\omega_2 = S \sqrt{32J_{II} \left(Z_g^2 J_{II} \alpha_{II} + \delta \frac{2J_I Z_g^2 \alpha_I + x_3}{4J_I Z_g^2 \alpha_I + \delta + 2x_3} \right)} \quad (9)$$

$$\omega_3 = S \sqrt{8J_I \left[2x_3 + \delta \left(1 - \frac{J_{I-II}}{J_I} + \frac{J_{II}}{J_I} \frac{2\delta}{\delta + 2x_3} \right) \right]} \quad (10)$$

$$\omega_4 = S \sqrt{8J_I \left[4Z_g^2 J_I \alpha_I + 2x_3 + \delta \left(1 - \frac{J_{I-II}}{J_I} + \frac{J_{II}}{J_I} \frac{2\delta}{\delta + 2x_3 + 4Z_g^2 J_I \alpha_I} \right) \right]}, \quad (11)$$

where $Z_g = 1 + \mathcal{O}(1/S) \approx 0.6$ is the quantum renormalization factor for the spin-wave anisotropy gap when

obtained from our data analysis, the details of which are discussed next, are summarized in Table II.

A Spin-wave theory

$$I \quad T=0$$

Our measured spin-wave energies can be explained within the framework of $T = 0$ interacting spin-wave theory (SWT). The theory is discussed in detail in Ref. 49. Here we give only a brief summary with the salient results. Starting from the spin structure shown in Fig. 1, we express each of the six spins (four Cu_I's and two Cu_{II}'s) in the unit cell by the Dyson-Maleev transformation for general spin S . The sums in \mathcal{H}_I and \mathcal{H}_{II} are then truncated at the harmonic order in the spin-wave boson operators. However, the \mathcal{H}_{int} term vanishes at the zone center, and therefore has effects only if one expands it to quartic order. We then approximate each product of four spin-wave operators by contracting operator-pairs in all possible ways. This yields new quadratic terms, whose coefficients contain the parameter $\delta = 2J_{I-II}\langle ae \rangle/S$, where a and e are boson operators associated with Cu_I and Cu_{II}, respectively. This coefficient contains the factor $1/S$, thus representing quantum corrections due to spin-wave interactions. The spin-wave energies are then found as the eigenvalues of the 6×6 matrix which arises from the resulting bilinear spin-wave Hamiltonian.⁴⁹

Since the magnetic unit cell contains 6 Cu spins, the spin-wave spectrum has six branches. Two of these are optical modes which are practically degenerate at $\omega = 4SZ_e J_I$. In this paper we will only discuss the remaining four modes. The large in-plane spin-wave velocity for the Cu_I spins makes it difficult to study the dispersion other than at the 2D zone center along the L direction, where the mode energies can be found analytically. The energies of these modes at $T = 0$ for wavevectors $(1 \ 0 \ L)$ are (in order of increasing energy)

$S = 1/2$, and $x_3 = Z_3^2 J_{I,3D} [1 + \cos(\pi L)]$, where $Z_3 = 1 + \mathcal{O}(1/S) \approx 0.9$. In Eqs. (8-11) we have kept only

terms up to $\mathcal{O}(1/S)$. Since $\delta = \mathcal{O}(1/S)$, this term is not renormalized. Note that the dispersion of ω_1 and ω_2 is of order δ , and hence is purely fluctuational. Note also that α_I and $J_{I,3D}$ appear always with the renormalization factors Z_g and Z_3 ; thus, we can only determine the products $Z_g^2\alpha_I$ and $Z_3^2J_{I,3D}$.

The physics of these modes can be deduced from the structure of the mode energies. Because only ω_2 and ω_4 involve the XY anisotropies, α_I and α_{II} , we see that these modes are out-of-plane modes, *i. e.* modes in which the spins oscillate out of the easy plane. Correspondingly, ω_1 and ω_3 are in-plane modes in which the spins move within the easy plane. In this connection note that the energies for ω_1 and ω_3 can be obtained from ω_2 and ω_4 , respectively, by omitting all factors which involve the XY anisotropies. Likewise, modes ω_3 and ω_4 involve J_I and are hence modes which primarily exist on the Cu_I sublattice (Cu_I modes), whereas modes ω_1 and ω_2 involve J_{II} and are modes which primarily exist on the Cu_{II} sublattice (Cu_{II} modes). From this it follows that the modes ω_1 and ω_2 will have high intensity near Cu_{II} Bragg positions and low intensity near Cu_I Bragg positions and conversely for the modes ω_3 and ω_4 . Finally, we should point out that $\omega_1 \rightarrow 0$ as $\mathbf{q} \rightarrow 0$ only because we have here neglected the small pseudodipolar interactions and four-fold anisotropy which lead to in-plane anisotropy.

One should be careful in determining the absolute value of the XY-anisotropy of the exchange coupling, since the quantum renormalization factor for the spin-wave gap (Z_g) is different from that of the spin-wave velocity (Z_c). Moreover, the value of Z_g is not known accurately. Z_g was first discussed by Barnes *et al.*⁵⁰ in their Monte Carlo study of a Heisenberg-Ising antiferromagnet. They discovered that the anisotropy gap was almost a factor of two smaller than that of the linear spin-wave prediction. In their series expansion study of the Heisenberg-Ising model, Zheng *et al.*⁵¹ calculated $Z_g = 0.635(10)$; Singh and Gelfand⁵² also calculated the renormalization of the Ising gap using the series expan-

sion method: $Z_g \approx 0.56$. This value agrees with Monte Carlo data from Ref. 50. On the other hand, Z_c has been known since Oguchi's work,⁵³ and a number of high-precision calculations of Z_c have become available recently. The series expansion results by Singh⁵⁴ and by Igarashi⁵⁵ are $Z_c = 1.176$ and $Z_c = 1.1794$, respectively. We use the Monte Carlo result of Beard *et al.*, $Z_c = 1.17$.⁶

As pointed out by Barnes *et al.*,⁵⁰ the factor Z_g can be physically understood by considering the effect of fluctuations.⁵⁶ Spin wave theory assumes a classical Néel ground state with a perfectly ordered moment, and the resulting dispersion relation is for the spin-waves propagating in such a background. Clearly, both quantum fluctuations and thermal fluctuations substantially reduce the ground-state alignment; long wavelength spin-waves thus see a "softened" antiferromagnetic background, and we see the renormalization of the gap, which is proportional to the staggered magnetization that is reduced from its classical value due to fluctuations. The effect of thermal fluctuations is well known from the studies of K_2NiF_4 and $\text{Sr}_2\text{CuO}_2\text{Cl}_2$, where the gap energy follows the temperature dependence of the order parameter. Analogously, quantum fluctuations also reduce the gap energy from the classical value even at zero temperature. In the $S = 1/2$ SLQHA, the zero temperature ordered moment is reduced by $\sim 40\%$. We use the renormalization $Z_g \sim 0.6$ from this fact.

2 Temperature dependence of the Mode Energies

As we shall see, fitting the experimentally determined mode energies to the expressions of Eqs. (9-11) suggests that the temperature dependence of δ is the same as that of $M_{s,II}^2$. Combining the zero temperature results with the random phase approximation results for $\delta = 0$ we propose to describe the mode energies at nonzero temperature (but for $x_3 = 0$) by

$$\omega_2^2 = 32J_{II}S_{II} \left(Z_g^2 J_{II} \alpha_{II} S_{II} + \frac{\delta_0 S_{II}^2}{S_I} \frac{2J_I Z_g^2 \alpha_I S_I}{4J_I Z_g^2 \alpha_I S_I + \delta_0 S_{II}^2 / S_I} \right) \quad (12)$$

$$\omega_3^2 = 8J_I \delta_0 S_{II}^2 \left(1 - \frac{J_{I-II}}{J_I} + 2 \frac{J_{II}}{J_I} \right) \quad (13)$$

$$\omega_4^2 = 8J_I S_I \left[4Z_g^2 J_I \alpha_I S_I + \frac{\delta_0 S_{II}^2}{S_I} \left(1 - \frac{J_{I-II}}{J_I} + \frac{J_{II}}{J_I} \frac{2\delta_0 S_{II}^2}{\delta_0 S_{II}^2 + 4J_I \alpha_I Z_g^2 S_I^2} \right) \right], \quad (14)$$

where $S_I \equiv S(1 - T/T_{N,I})^{\beta_I}$, $S_{II} \equiv S(1 - T/T_{N,II})^{\beta_{II}}$, and δ_0 is the value of δ for $T = 0$.

B $T > T_{N,II}$

At high temperatures ($T \gg T_{N,II}$), we can ignore the Cu_{II} 's and treat the Cu_I system as a two-sublattice anti-

ferromagnet. We also require that $T \ll T_{N,I}$, so that we can ignore the T -dependence of the Cu_I moment. Setting $\delta = 0$, $\omega_{\perp} = \omega_4$ near the $(1\ 0\ L)$ magnetic reciprocal

position is given by

$$\omega_{\perp} = 4SJ_I \left[2Z_g^2 \alpha_I + Z_c^2 \frac{(q_{2D}a)^2}{4} + Z_3^2 \frac{J_{I,3D}}{J_I} (1 + \cos(\pi L)) \right]^{1/2}. \quad (15)$$

Here, q_{2D} is the momentum transfer in the plane, $q_{2D} \equiv \frac{2\pi}{a} \sqrt{(H-1)^2 + K^2}$, and a is the lattice constant. Note that the distance between the Cu_I - Cu_I nearest neighbors is $a/\sqrt{2}$. The in-plane mode, $\omega_{\parallel} = \omega_3$, has the same dispersion relation, with α_I replaced by zero, because we assume zero in-plane anisotropy.

From a measurement of the spin-wave dispersion along $[1\ 0\ L]$, it is then possible to extract both α_I and $J_{I,3D}$, using Eq. (15). In Fig. 6, such measurements are shown. We have chosen a relatively high temperature of $T = 200\text{K} \approx T_{N,I}/2$ in order to take advantage of the magnon population factor $n(\omega)$ in the cross section. The experiment was carried out in the constant- \mathbf{Q} mode, in which the final neutron energy was fixed at $E_f = 14.7\text{meV}$ and the spectrometer was set to operate in the neutron energy loss configuration. A horizontal collimation sequence 20° - 40° - S - 80° - 80° was employed, which resulted in energy resolutions (full width) between ~ 1.4 and $\sim 1.7\text{meV}$ for energy transfers between 3 and 12meV. In this figure, $(1\ 0\ \bar{1})$ is the zone center and $(1\ 0\ \bar{2})$ is the zone boundary. In order to show that the gap of $\sim 5\text{meV}$ at the zone center $(1\ 0\ \bar{1})$ is indeed an out-of-plane mode, we compared the $(1\ 0\ \bar{1})$ data with the scan at the $(1\ 0\ \bar{5})$, where the intensity of an out-of-plane mode would be reduced due to the geometric factor $\sin^2 \phi$ in Eq. (5).

We have analyzed our data by convolving the spin-wave cross section, Eq. (5), with the resolution function of the spectrometer. Attempts to fit the data with a single peak are not successful. Figure 7(a) shows a summary of our results for the dispersion of the Cu_I modes ω_3 and ω_4 at $T = 200\text{K}$, along the L -direction. The filled circles denote the in-plane mode and the open circles the out-of-plane mode. Fixing $J_I = 130\text{meV}$ and $\delta = 0$, we fit the gapless data to ω_3 [Eq. (10)], and obtain $J_{I,3D} = 0.14(2)\text{meV}$. Compared to $J_I \simeq 130\text{meV}$, the inter-planar coupling is rather small: $J_{I,3D}/J_I \approx 1.1 \times 10^{-3}$. However, this $J_{I,3D}/J_I$ value is larger than those in $\text{Sr}_2\text{CuO}_2\text{Cl}_2$ and La_2CuO_4 , where copper oxide planes are stacked differently. Namely, the interplanar interaction is not frustrated in $\text{Sr}_2\text{Cu}_3\text{O}_4\text{Cl}_2$, whereas in the other compounds it is frustrated.

We then fit the out-of-plane data to Eq. (11) and find $\alpha_I = 5.2(9) \times 10^{-4}$. In their study of $\text{Sr}_2\text{CuO}_2\text{Cl}_2$, Greven *et al.*⁷ determined the XY-anisotropy in J_I as $\alpha_{2122} = 1.4(1) \times 10^{-4}$, without recognizing the different quantum renormalization factor for the spin-wave gap (Z_g). If α_{2122} is multiplied by $(Z_c/Z_g)^2$, it becomes $5.3(4) \times 10^{-4}$, which is consistent with our α_I . This XY anisotropy has been explained by Yildirim *et al.*⁵⁷ as resulting from a combination of spin-orbit and Coulomb

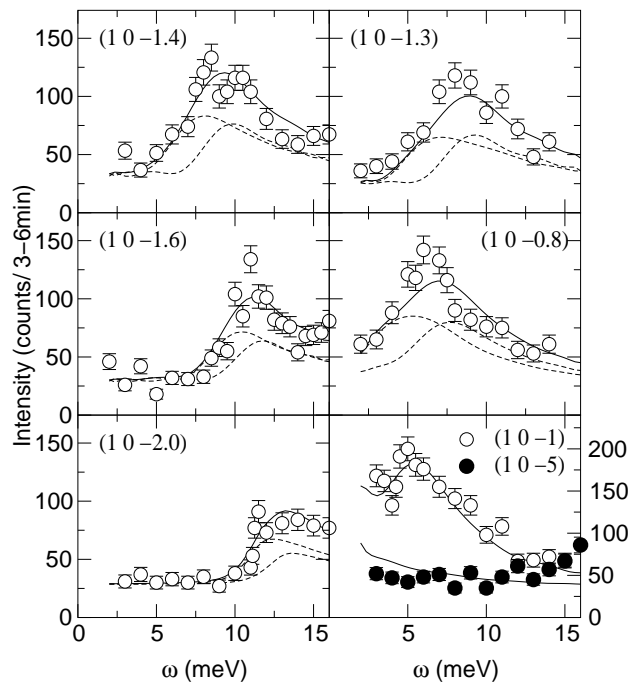


FIG. 6: Representative inelastic neutron scattering intensity from Cu_I spin waves (ω_3 and ω_4). Each panel shows a scan at $T = 200\text{K}$ with the momentum transfer \mathbf{Q} fixed as noted. The solid line is the cross section, Eq. (5), convoluted with the experimental resolution function. The dashed lines indicate the individual contributions of the two spin-wave modes to the overall intensity.

exchange interactions.

Note that the solid lines in Fig. 6 are produced with fixed J_I , α_I , and $J_{I,3D}$, while the dashed lines indicate the individual contributions of the two spin-wave modes to the overall intensity. The \mathbf{Q} -dependence of the scattering intensity only comes from the geometric factor and the spin-wave dispersion; thus, we are able to use a single set of parameters in Eqs. (5-6) to explain the observed cross sections for various \mathbf{Q} 's in Fig. 6.

We next discuss the temperature dependence of the out-of-plane gap. In previous studies of the tetragonal SLQHA K_2NiF_4 ($S = 1$)³⁶ and $\text{Sr}_2\text{CuO}_2\text{Cl}_2$ ($S = 1/2$),⁷ it has been found that the gap energies exhibit the same temperature dependences as the respective order parameters throughout the entire ordered phase. As discussed above in Sec. IV A, this is due to the softening of the antiferromagnetic background by thermal fluctuations. Figure 8 shows constant- \mathbf{Q} scans at various temperatures at the Brillouin zone center $(1\ 0\ \bar{1})$. The data can be fitted well with Eq. (5); the fitting results are shown as solid lines in the figure. Due to the steep in-plane dispersion, the fitted gap energy, indicated by the arrows, is slightly smaller than the apparent peak position, and the peaks appear to have wider widths than the resolution.

The summary plot in Fig. 9 clearly shows the change

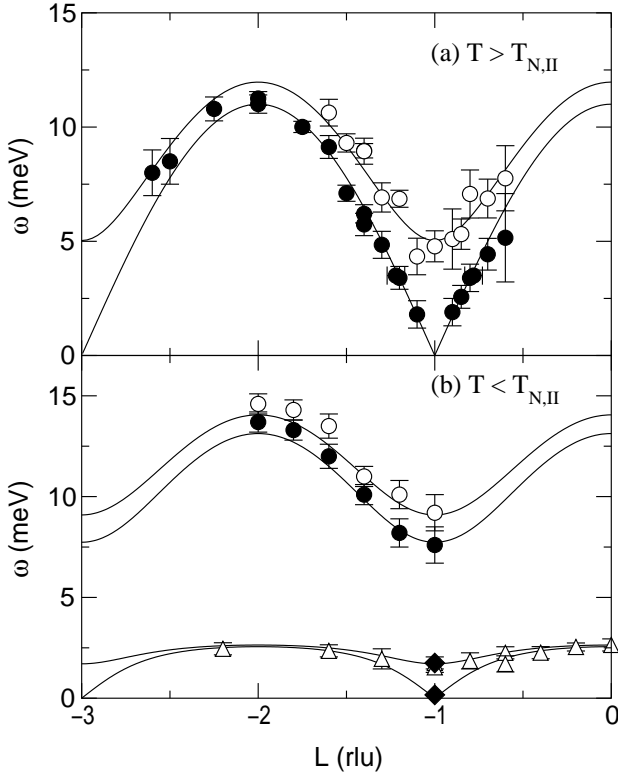


FIG. 7: (a) Spin-wave dispersion of ω_3 and ω_4 along $(1\ 0\ L)$ at $T=200\text{K}$. Filled circles denote ω_3 and open circles ω_4 extracted from fitting the data. The solid lines are the dispersion relations, Eq. (10) and Eq. (11). (b) ω_3 and ω_4 at $T=30\text{K}$, and ω_2 at $T=12\text{K}$. The solid lines are the dispersion relations, Eq. (8-11). ω_2 is shown in open triangles. Filled diamonds are results from antiferromagnetic resonance experiment by Katsumata *et al.*⁴⁸

of the gap energy as a function of temperature. As expected, ω_4 follows the Cu_I order parameter from $T_{N,I} \approx 40\text{K}$ up to $T_{N,II}$. However, a large increase is observed below $T_{N,II}$. Further new low-energy features appear below 40K . We discuss this dramatic behavior of the long-wavelength spin-waves below 40K in the next subsection.

C $T < T_{N,II}$

The dramatic behavior of the low-energy, long-wavelength spin waves at $T < T_{N,II}$ results from the effective biquadratic interaction, δ , produced by quantum fluctuations. We now discuss the effect of δ on the spin-wave energies on the basis of Eqs. (8-11). The energy of the out-of-plane mode ω_4 increases dramatically as the Cu_{II} spins order and δ comes into play. For the in-plane mode the effect of δ is even more dramatic because in the absence of in-plane anisotropy, its energy is zero for $\delta = 0$. The existence of the out-of-plane mode ω_2 requires

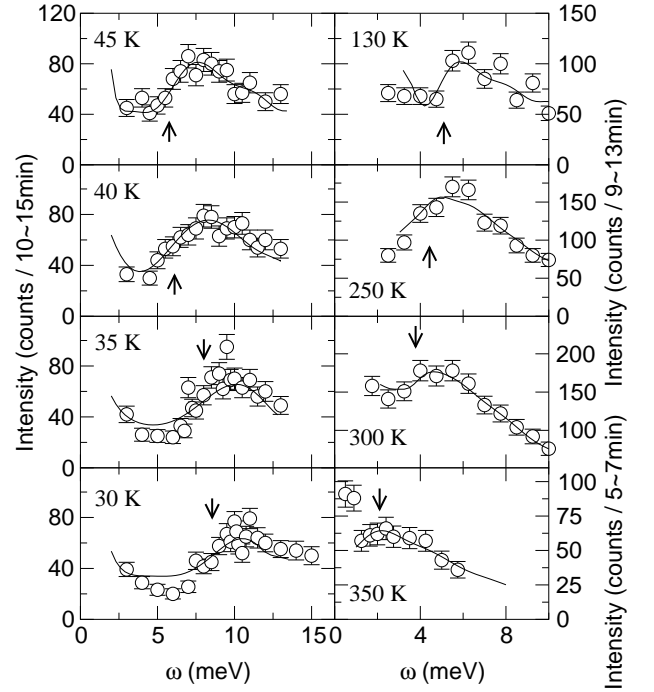


FIG. 8: Constant- Q scans at the 3D zone center $(1\ 0\ \bar{1})$ at various temperatures. Solid lines are fits to Eq. (5). Arrows denote the gap energies extracted from the fits. The final neutron energy was fixed at 14.7 meV and collimations of $20^\circ\text{-}40^\circ\text{-S-}20^\circ\text{-}40^\circ$ were used. At high temperatures, tighter collimations were used to improve the energy resolution.

long-range order of the Cu_{II} subsystem. Here nonzero δ causes an increase in the out-of-plane anisotropy (from $J_{II}\alpha_{II}$ to approximately $J_{II}\alpha_{II} + 2J_I\alpha_I$) because the quantum fluctuations strongly couple the two subsystems. As mentioned above, the effective biquadratic exchange does not create an energy gap in the mode ω_1 .

1 The Cu_I -like modes

The peak in our data for $T < 40\text{K}$, in Fig. 8, is identified as an overlap of peaks from the ω_3 and ω_4 modes. These spin-wave modes could not be resolved due to both the steep in-plane dispersion of the Cu_I -like mode and the existence of a nearby phonon peak. However, one can obtain indirect evidence for the correctness of this description by exploiting the different polarizations of the ω_3 and ω_4 modes. In Fig. 10(a), we compare scans at the $(1\ 0\ \bar{1})$ position and the $(1\ 0\ 7)$ position. The data at the $(1\ 0\ \bar{1})$ position can be satisfactorily fitted with both a single peak and two peaks. Specifically, the dashed line in Fig. 10(a) assumes δ is zero in Eq. (10), so that there is only one energy gap from ω_4 . The solid line assumes non-zero δ , thus producing a double peak feature: both

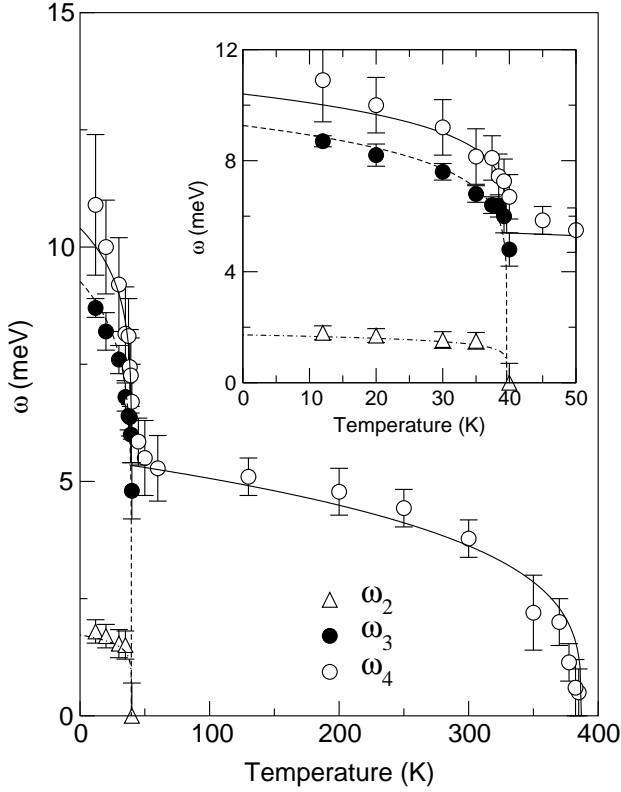


FIG. 9: Temperature dependence of the spin-wave gap at the 3D zone center $(1\ 0\ \bar{1})$. Open triangles, filled circles and open circles denote ω_2 , ω_3 , and ω_4 , respectively. Solid, dashed, and dot-dashed lines represent respective spin-wave calculation, Eq. (12-14). Inset: Same data plotted in a different scale to magnify the low temperature region.

ω_3 and ω_4 . Using the same set of parameters obtained from fitting the $(1\ 0\ \bar{1})$ data, we plot the solid and dashed lines for the peak profile at $(1\ 0\ \bar{7})$. Evidently, an in-plane gap (ω_3) is necessary to explain the data at $(1\ 0\ \bar{7})$, where the contribution of the out-of-plane mode becomes very small due to the geometric factor. Therefore, we have shown that this peak below 40K results from an overlap of ω_3 and ω_4 . We have, therefore, fitted all of the data assuming that there are two modes. We emphasize that for $T < T_{N,II}$, the non-zero energy of $\omega_3(\mathbf{q} = 0)$ is a pure quantum effect; the close values of ω_3 and ω_4 simply reflect the fact that the effective anisotropy associated with δ is larger than the intrinsic Cu_I out-of-plane anisotropy α_I [see Eqs. (10) and (11)], thus illustrating the quantitative importance of *quantum fluctuations*.

We have measured the dispersion along the L -direction of the ω_3 and ω_4 modes for $T < T_{N,II}$. Each scan is fitted with the cross section containing both ω_3 and ω_4 . The fitting results are shown in Fig. 7(b) as filled and open circles for ω_3 and ω_4 , respectively. The solid lines in Fig. 10(b) are drawn using Eqs. (10-11) and (13-14), with $\delta_0 =$

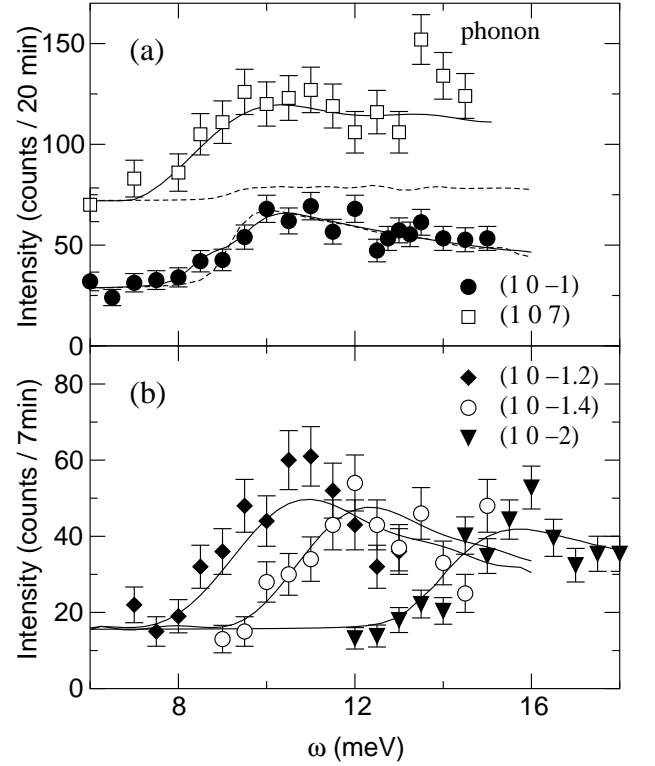


FIG. 10: (a) Constant- Q scan of the spin-wave gap at the 3D zone center at 10K. The $(1\ 0\ \bar{1})$ scan shows an overlap of in-plane (ω_3) and out-of-plane (ω_4) mode, while the scan at $(1\ 0\ \bar{7})$ is almost entirely in-plane mode, due to the geometric factor of the neutron cross section. The baseline of the $(1\ 0\ \bar{7})$ data is offset by 50. The solid and dashed curves are fits for two peaks and one peak, respectively. (b) Dispersion along L of Cu_I -like modes at $T=30\text{K}$.

$0.26(4)\text{meV}$ determined by fitting ω_3 with fixed $J_I = 130\text{meV}$. Note that we have assumed the temperature dependence of δ as discussed in Sec. IV A 2. Using the theoretical relation $\delta_0 = 0.3372J_{I-II}^2/J_I = 0.26$ from Ref. 49, we obtain $|J_{I-II}| = 10(2)\text{meV}$, in excellent agreement with the earlier magnetization study.²⁰

2 The Cu_{II} -like modes at $(1\ 0\ \bar{1})$

The low-energy mode that appears at temperatures below 40K is attributed to ω_2 . At least two experimental observations support this identification. In Fig. 11(a), we compare this mode at different L positions; the peak evident at the $(1\ 0\ \bar{1})$ position disappears at the $(1\ 0\ \bar{7})$ position, thus proving that this gap is an out-of-plane mode. Next, in order to show that this mode is Cu_{II} -like, the $(1\ 0\ \bar{1})$ scan is compared with the scan at the $(1.02\ 0\ \bar{1})$ position in Fig. 11(b). Although there is no discernible peak at $(1.02\ 0\ \bar{1})$, the remaining intensity

is consistent with the calculation using the Cu_{II} spin-wave velocity ($\sim 95\text{meV}\text{\AA}$). If the Cu_I spin-wave velocity ($\sim 830\text{meV}\text{\AA}$) is used instead, the dashed line is obtained, which is basically at the background level. Therefore, this low-energy feature is the Cu_{II} -like out-of-plane mode: ω_2 .

In Fig. 11(c), the temperature dependence of the ω_2 gap at the $(1\ 0\ \bar{1})$ position is shown. As expected, the ω_2 gap vanishes for $T > 40\text{K}$. The temperature dependence of ω_2 is summarized in Fig. 9 as open triangles. The lines in Fig. 9 correspond to Eqs. (12-14). The agreement between the calculation and the experimental results over the entire temperature range is excellent, if one takes into account the inherent difficulty in resolving ω_4 and consequent large error bars for ω_4 .

The dispersion of ω_2 along L at $T = 12\text{K}$ is shown in Fig. 11(d); the summary is plotted in Fig. 7(b) as open diamonds. The solid lines in Fig. 7(b) for ω_1 and ω_2 have no adjustable parameters; all the parameters have been determined independently from separate measurements. We set $\alpha_{II} = 0$, since our least square fit of the data to Eq. (9) yields $\alpha_{II} = 0.0001(5)$, which is indistinguishable from zero.

The ω_1 mode could not be identified as a distinct mode in our experiment, due to the presence of an acoustic phonon. Note that the $(1\ 0\ \bar{1})$ position is a nuclear Bragg position as well as a magnetic zone center. However, in a recent study, Katsumata *et al.*⁴⁸ reported an observation of antiferromagnetic resonance modes at $T=1.5\text{K}$ using the ESR techniques. They showed that there are two modes: an out-of-plane mode at 422.5GHz ($\sim 1.75\text{meV}$) in good agreement with our ω_2 value [$\omega_2(T \rightarrow 0) \approx 1.72\text{meV}$], and an in-plane mode at 36.1GHz ($\sim 0.15\text{meV}$), which is too small to be observed with thermal neutrons. These results are plotted as filled diamonds in Fig. 7.

Therefore, the combined inelastic neutron scattering results and spin-wave calculations in Figs. 7 and 9 clearly demonstrate the success of our model Hamiltonian in explaining the observed temperature and momentum dependences of the spin-waves.

3 The Cu_{II} -like modes at $(1/2\ 1/2\ 0)$

The discussion so far has been of the excitations observable near the reciprocal lattice vector $(1\ 0\ \bar{1})$, the Cu_I magnetic Bragg peak position. Unlike the spin-wave energy, which depends only on the reduced wave vector $\mathbf{q} = \mathbf{Q} - \mathbf{G}$, the neutron scattering intensity from spin waves depends also on the reciprocal lattice vector \mathbf{G} . The neutron scattering intensity is strong near an antiferromagnetic \mathbf{G} , or $(\pi\ \pi)$ position, while it is weak near a nuclear Bragg position, $(0\ 0)$. From the spin-wave calculation, we have found that the Cu_{II} -like modes have very large intensity near the Cu_{II} magnetic Bragg position, while the Cu_I -like modes have vanishingly small

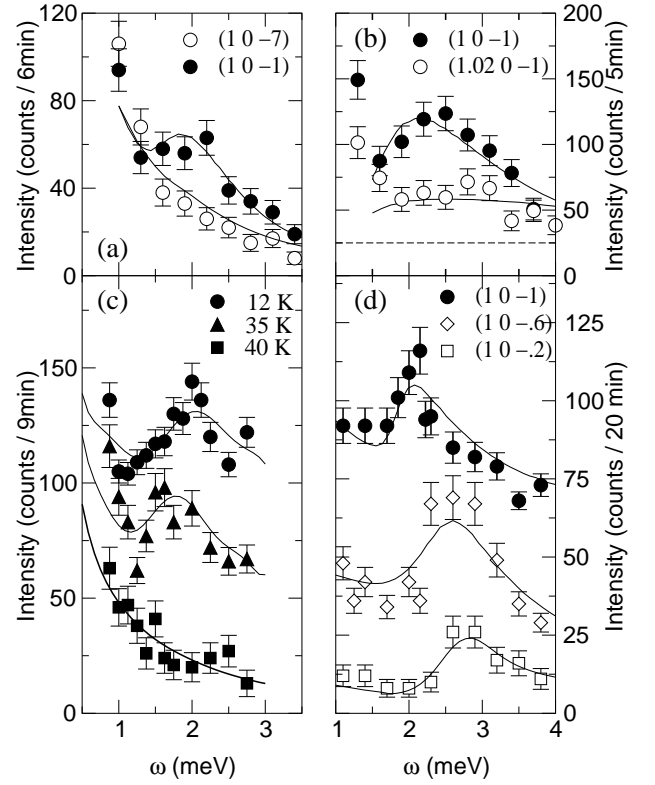


FIG. 11: (a) Comparison of ω_2 gap at $(1\ 0\ \bar{1})$ and $(1\ 0\ \bar{7})$, showing that ω_2 is an out-of-plane mode. Experimental configuration: $E_i = 14.7\text{meV}$, collimation sequence of $40^\circ\text{-}40^\circ\text{-S-}40^\circ\text{-}80^\circ$, at $T = 35\text{K}$. (b) Comparison of ω_2 gap at two slightly different in-plane wave vectors. Experimental configuration: $E_f = 14.7\text{meV}$, $60^\circ\text{-}60^\circ\text{-S-}60^\circ\text{-}40^\circ$, at $T = 10\text{K}$. (c) Temperature dependence of ω_2 gap at $(1\ 0\ \bar{1})$. Experimental configuration: $E_i = 14.7\text{meV}$, $40^\circ\text{-}40^\circ\text{-S-}20^\circ\text{-}80^\circ$. (d) Scans showing a small dispersion of ω_2 along L . Experimental configuration: $E_i = 13.7\text{meV}$, $20^\circ\text{-}40^\circ\text{-S-}20^\circ\text{-}40^\circ$, at $T = 12\text{K}$. All solid lines are fits to Eq. (9). Dashed curve in (b) is the same as that for $(1.02\ 0\ \bar{1})$, but using the Cu_I spin wave velocity.

intensity. Although the Cu_{II} -like modes have large intensity near $(1/2\ 1/2\ L)$, as illustrated in Fig. 12(a), a rather complex dispersion relation results due to the presence of different magnetic domains (see Fig. 3). Spin-waves from domain A are shown as dashed lines, while those from domain B are shown as solid lines in the figure. Therefore, one expects to observe three or four peaks within an 1meV range around $\omega = 2.5\text{meV}$ from neutron scattering; this is an extremely difficult task, considering that the experimental resolution is about $0.2 \sim 0.3\text{meV}$ in this energy range with cold neutrons.

Representative scans are plotted in Fig. 12(c); the data have been taken at the SPINS spectrometer at the NCNR with collimations of $30^\circ\text{-}80^\circ\text{-S-}80^\circ\text{-}100^\circ$, and with the final neutron energy fixed at 5meV . The solid line and the

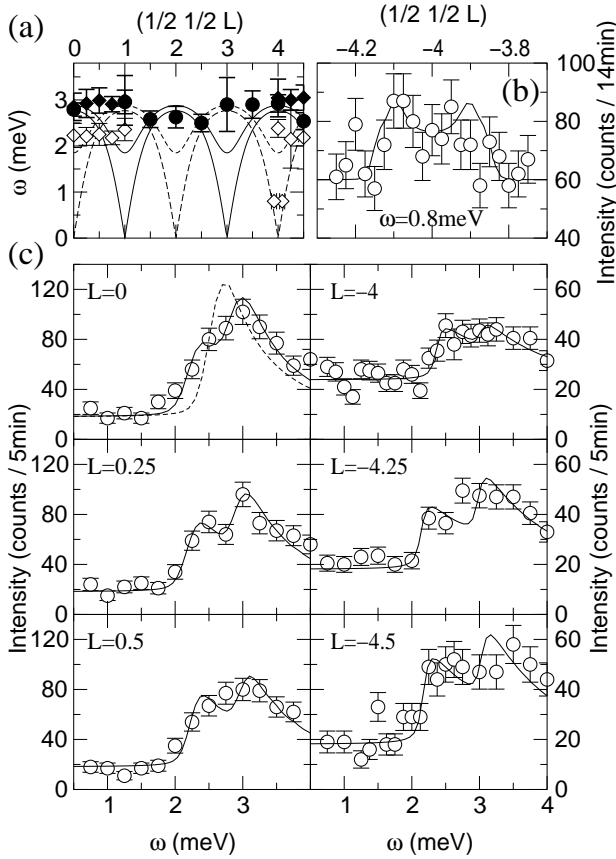


FIG. 12: (a) Spin-wave dispersion of the Cu_{II} -like modes along the L -direction near the Cu_{II} antiferromagnetic Bragg position $(1/2 \ 1/2 \ L)$. Since different magnetic domains have different reciprocal lattice vector (see Fig. 3), rather complicated dispersion relations result. Spin-waves from domain A are shown as dashed lines, while those from domain B are shown as solid lines. (b) Constant- ω scan of the ω_1 mode near the $(1/2 \ 1/2 \ \bar{4})$ position. Solid lines are fits to Eq. (8), and the fitted L value of the peak is plotted in part (a) as open diamonds. (c) Constant- Q scans of the Cu_{II} -like modes.

dashed line for the $L = 0$ data are the results of fits to two spin-wave modes and one spin-wave mode, respectively. The two-mode fit is clearly better than the one-mode fit. Fitting current data with three spin-wave modes yields no meaningful results, since the error bars are larger than the separation in peak energies. Therefore, all data have been fitted with two spin-wave modes, and the results of this fitting are plotted as the solid and open diamonds in Fig. 12(a). The solid circles in Fig. 12(a) are the fitting results from coarse resolution measurements using higher energy neutrons. A constant- ω scan is shown in Fig. 12(b) near the $(1/2 \ 1/2 \ \bar{4})$ position at $\omega = 0.8$ meV. The solid line is a fit to Eq. (8). Since ω_1 is an in-plane mode, we are able to observe this at large L values.

From these data, we can establish the following: First,

the constant- Q scan reveals that there is more than one mode in the 2 to 3 meV energy range, roughly coinciding with the theoretical prediction. Note that the theoretical prediction, shown as solid and dashed lines in Fig. 12(a), is obtained with parameters determined from previous sections, and thus contains no adjustable parameters. Second, in agreement with the theoretical prediction, one of these modes is an in-plane mode and the other an out-of-plane mode. However, more experiments with higher resolution will be valuable in understanding the observed spin-wave dispersion.

D Spin-wave dispersion of Cu_{II} in the plane

Because J_{II} is relatively small, the Cu_{II} zone-boundary spin-wave energies are low enough to be accessed with thermal neutrons. We have measured spin-waves in the ab -plane, along the high-symmetry directions. The experiment was conducted at 10K, which is well below $T_{N,II}$, and in the $(H \ K \ 0)$ zone; that is, ab -plane is in the scattering plane. Both constant- ω scans and constant- Q scans were carried out. Some typical constant- ω scans, along the $[1 \ 1 \ 0]$ direction, are shown in Fig. 13(a). The solid lines are obtained from a least-square fit to the cross section, convoluted with the instrumental resolution. Examples of constant- Q scans along the zone boundary are shown in Fig. 13(b).

Our zone boundary data exhibit a double-peak structure. The feature at the high energy is the spin-wave, while the low-energy feature is a phonon. We have verified the different nature of the scattering of the two features by measuring the respective peak intensities at equivalent reciprocal lattice positions with larger $|\mathbf{Q}|$. Such measurements at $(\frac{3}{2} \ 1 \ 0)$, $(\frac{5}{2} \ 1 \ 0)$, $(\frac{7}{2} \ 1 \ 0)$, and $(\frac{9}{2} \ 1 \ 0)$ are shown in Fig. 13(c): The intensity of the low-energy feature increases approximately as $\sim |\mathbf{Q}|^2$, characteristic of phonon scattering, while the intensity of the second feature is nearly independent of $|\mathbf{Q}|$.

Figure 14 summarizes our results. From the zone boundary spin-wave energy of 25meV one can deduce J_{II} rather accurately as $J_{II} = 10.5(5)$ meV, in excellent agreement with the value deduced in Ref. 20 from the Cu_{II} susceptibility. The gap energy at the zone center, ~ 3 meV, corresponds to the modes found at $L = 0$ in Fig. 12. Away from the 2D zone center, ω_1 and ω_2 from both domains are degenerate and can be approximated as the excitations of a simple SLQHA with the exchange interaction J_{II} . The long-wavelength effects of the spin-wave interactions can be absorbed into an effective anisotropy α_{II}^{eff} . With $\alpha_{II} \approx 0$, Eq. (9) can be interpreted as resulting from an effective anisotropy given by $J_{II}\alpha_{II}^{eff} = 2J_{II}\alpha_I\delta/(4J_{II}\alpha_I + \delta) \approx 0.1$ meV, or $\alpha_{II}^{eff} \approx 0.01$.

Simple linear SWT with $\alpha_{II}^{eff} = 0.01$ and $J_{II} = 10.5$ meV gives the dashed line in Fig. 14. This is a good approximation, except for the dispersion near the zone

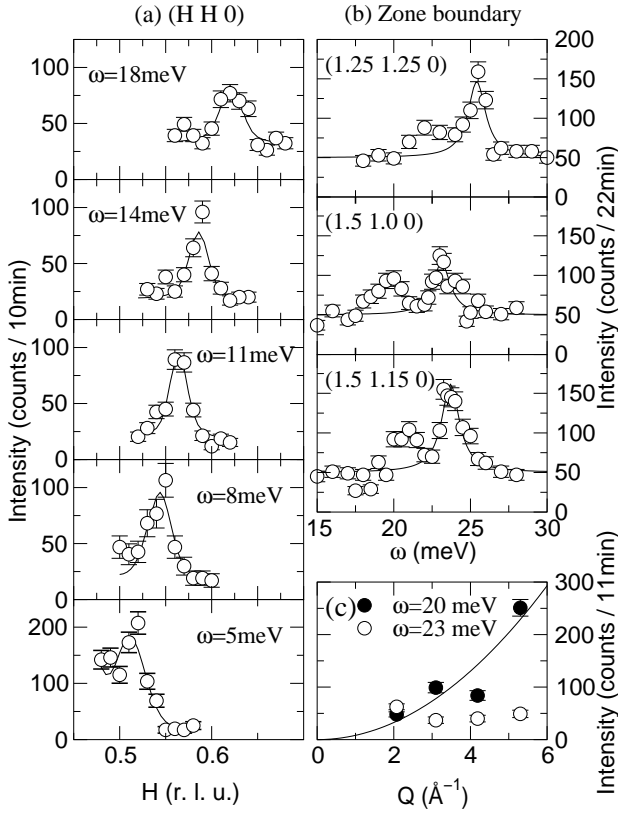


FIG. 13: (a) The constant- ω scan of Cu_{II} spin-waves at $T = 10\text{K}$ along the high-symmetry direction (H H 0). The 2D zone center ($\pi \pi$) and zone boundary ($\pi/2 \pi/2$) correspond to $\mathbf{Q}=(0.5 \ 0.5 \ 0)$ and $(0.75 \ 0.75 \ 0)$, respectively. (b) Constant- Q scans along the zone boundary. The $(1.5 \ 1.0 \ 0)$ is a local minimum and corresponds to $(\pi \ 0)$. (c) The $|Q|$ dependence of each peak in (b) at the $(1.5 \ 1.0 \ 0)$ or equivalent positions, which confirms the low-energy (20meV) feature as a phonon.

edge ($\pi \ 0$). As seen by the continuous line, our data are in much better agreement with a recent series expansion prediction by Singh and Gelfand.⁵² This theory predicts a local minimum at the zone boundary position ($\pi \ 0$), lower by about 7% than the value at $(\frac{\pi}{2} \ \frac{\pi}{2})$. A non-zero dispersion along the zone boundary may also result from a non-zero next-nearest-neighbor interaction J_{II}^{nnn} , within linear SWT. The magnitude of the dispersion between $(\pi \ 0)$ and $(\frac{\pi}{2} \ \frac{\pi}{2})$ is given by $2SJ_{II}^{nnn}$. Considering that J_{II} is already of order 10 meV and the next-nearest-neighbor distance is large ($\sim 7.7\text{\AA}$), it is unlikely that the next nearest neighbor effects contribute strongly to the observed zone-boundary energy difference of $\sim 2\text{meV}$ in $\text{Sr}_2\text{Cu}_3\text{O}_4\text{Cl}_2$.

Therefore, this dispersion can be regarded as a pure quantum mechanical effect for the $S = 1/2$ nearest neighbor Heisenberg model. Canali *et al.*⁵⁸ obtained similar but smaller zone boundary dispersion in their higher or-

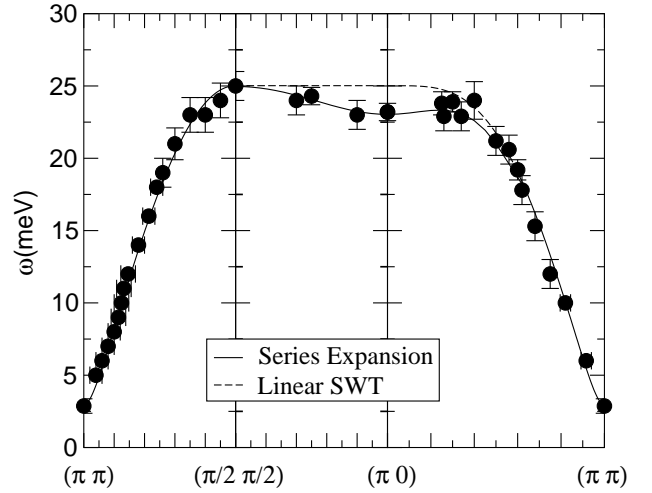


FIG. 14: Cu_{II} in-plane spin-wave dispersion at $T = 10\text{K}$. The dashed line is a fit to the linear SWT with $J_{II} = 10.5\text{meV}$ and $\alpha_{II}^{eff} \approx 0.01$. The solid line is the series expansion result (Ref. 52) with the same values for J_{II} and α_{II} .

der SWT. They calculated the correction to Z_c up to $1/S^2$ order, and found that the correction is not uniform along the zone boundary, giving $\sim 2\%$ dispersion. In their spin-rotation-invariant theory, Winterfeldt and Ihle⁵⁹ also obtained a local minimum at the $(\pi \ 0)$ position which is smaller than the energy at the $(\frac{\pi}{2} \ \frac{\pi}{2})$ position by almost 10%. Recent quantum Monte Carlo study by Syljuåsen and Rønnow⁶⁰ also gives similar zone boundary dispersion of 6%, in good agreement with the series expansion result and our experimental result.

V. MAGNETIC CORRELATION LENGTH

The static structure factor provides valuable information about thermodynamic quantities such as the correlation length. As discussed in Sec. II, the necessary energy integration can be done automatically, in low-dimensional systems, via a 2-axis neutron scattering technique. In this section, we present our neutron scattering results from such 2-axis measurements, for both the Cu_I and Cu_{II} subsystems at temperatures higher than their respective Néel temperatures.

A Cu_I system

The magnetism above $T_{N,I}$ of the Cu_I system is essentially the same as that of La_2CuO_4 or $\text{Sr}_2\text{CuO}_2\text{Cl}_2$. The difference in the inter-plane coupling is not important at temperatures well above $T_{N,I}$. The only difference is the antiferromagnetic superexchange J_I , which is estimated

TABLE III: The Cu–O–Cu superexchange interaction and lattice constants of cuprates

	La ₂ CuO ₄	Sr ₂ CuO ₂ Cl ₂	Sr ₂ Cu ₃ O ₄ Cl ₂
a (Å)	3.81	3.967	3.86
J_I (meV)	132(4) ^a	125(6) ^b	130(5)

^aRef. 61

^bRef. 7

to be 132(4)meV for La₂CuO₄ from the neutron scattering experiment.⁶¹ Greven *et al.*⁷ extracted 125(6)meV for Sr₂CuO₂Cl₂ from the two magnon Raman scattering experiment by Tokura and coworkers.⁶² The Cu–O–Cu superexchange energies as well as in-plane lattice constants in these materials are compared in Table III, where the value for J_I in Sr₂Cu₃O₄Cl₂ is extracted from our correlation length data.

The cross section for an energy integrating scan across the Cu_I 2D fluctuations is given by

$$I(q_{2D}) \approx \int_{-\infty}^{E_i} d\omega S(\mathbf{Q}, \omega) \quad (16)$$

$$\approx [(\sin^2 \phi) S^T(q_{2D}) + (\sin^2 \phi + 2\cos^2 \phi) S^L(q_{2D})],$$

where $q_{2D} \equiv \frac{2\pi}{a}|H-1|$, and S^T and S^L are the transverse and longitudinal components of the static fluctuation. Here ϕ is the angle between \mathbf{Q} and $[0\ 0\ 1]$. At temperatures well above $T_{N,I}$ only the Heisenberg term is relevant in the Hamiltonian. In this regime the system is effectively isotropic; that is, $S^T \approx S^L$.

The neutron scattering data shown in Fig. 15 were obtained with the incoming neutron energy fixed at $E_i = 36.4$ meV and a collimation sequence of 10°–13°–S–10°. Higher order neutrons were filtered by both PG and sapphire filters. The data were fitted to a simple 2D Lorentzian convoluted with the instrumental resolution:

$$S(q_{2D}) = \frac{S_0 \kappa^2}{q_{2D}^2 + \kappa^2}, \quad (17)$$

where the width of the Lorentzian $\kappa \equiv \xi^{-1}$ is equal to the inverse correlation length.

The fitting results for the inverse correlation length, κ , are shown in Fig. 16(a) as open diamonds. We have also used $E_i = 13.7$ meV neutrons to improve the resolution at lower temperatures; these results are shown as open circles in the same plot. We also plot the quantum Monte Carlo data from several studies.^{6,39,64} The solid line is the renormalized classical (RC) expression of the QNL σ M:⁶⁵

$$\frac{\xi}{a} = \frac{e v/a}{8 \cdot 2\pi\rho_s} \exp\left(\frac{2\pi\rho_s}{T}\right) \left[1 - 0.5\frac{T}{2\pi\rho_s} + O\left(\frac{T}{2\pi\rho_s}\right)^2\right], \quad (18)$$

where ρ_s is the spin stiffness constant and v is the spin-wave velocity. For the $S = 1/2$ SLQHA, a recent Monte Carlo study by Beard *et al.*⁶ obtains $\rho_s/J = 0.1800(5)$

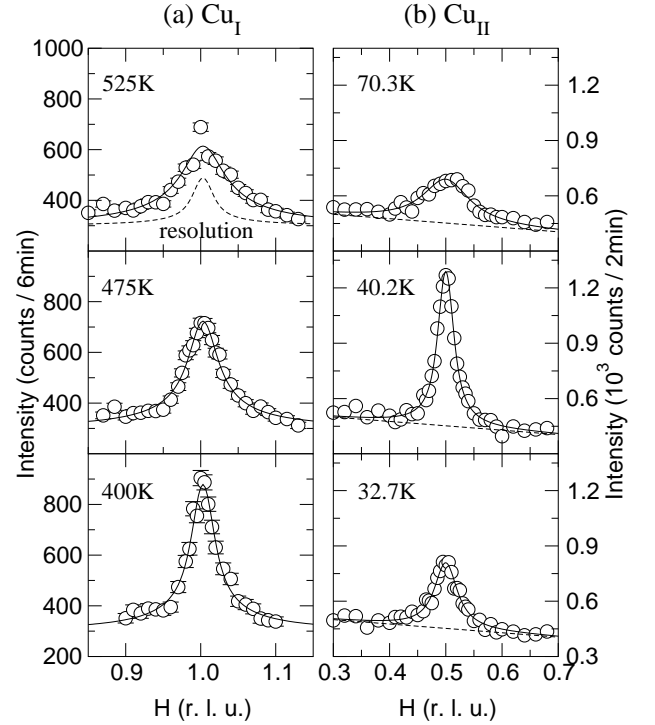


FIG. 15: Representative energy-integrating two-axis scans. The solid lines are fit to simple Lorentzians, Eq. (17). (a) Scans across the Cu_I 2D magnetic rod at (H 0.327); the dashed line shows the instrumental resolution. (b) Scans across the Cu_{II} 2D magnetic rod at (H 0.253); the dashed lines indicate the temperature independent background.

and $v/Ja = 1.657(2)$, and we have used these values substituted into Eq. (18) to obtain the solid line in Fig. 16(a). Although our data have large error bars, the general agreement between our experimental results and both theoretical results is quite good. We extract the value of J_I by comparing our data with quantum Monte Carlo results: $J_I = 130(5)$ meV. The experimental data deviate from the 2D Heisenberg prediction as the temperature approaches $T_{N,I}$ from above, since the system crosses over to 3D Heisenberg behavior due to the inter-plane coupling $J_{I,3D}$. We also show the fitting results for the Lorentzian amplitude $S_0\kappa^2 = S_0/\xi^2$ in Fig. 16(b). For the QNL σ M,³ this quantity is predicted to behave as $\sim T^2$ at low temperatures, while various neutron scattering studies^{7,8} reveal the empirical behavior $S_0/\xi^2 \sim \text{constant}$. Our data are compared with these two scaling behaviors in Fig. 16(b). The solid line is $\sim T^2$, while the dashed line is a constant; these lines are rescaled to fit the data. One should, however, note that the low temperature data (below 400K) probably do not show true 2D Heisenberg behavior but a crossover to 3D Heisenberg behavior, and they should be excluded in the comparison. Within experimental error bars, both lines

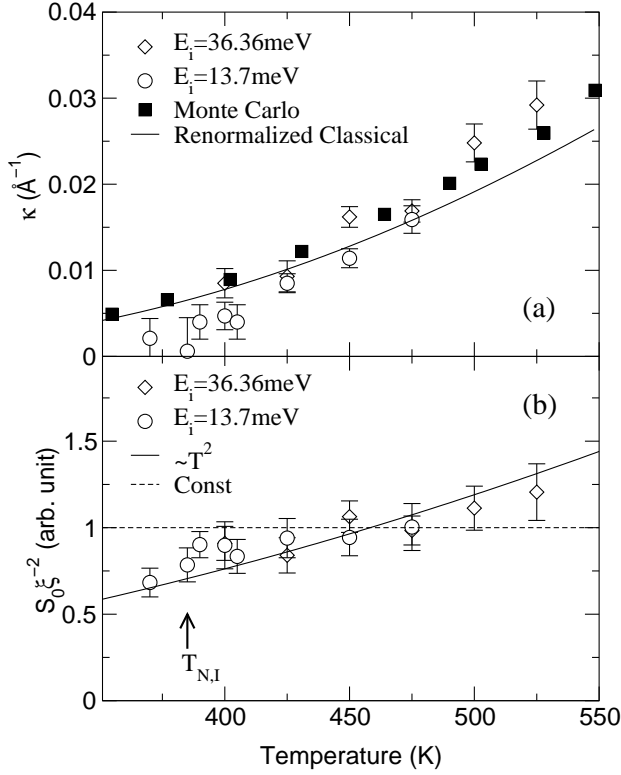


FIG. 16: (a) Inverse magnetic correlation length and (b) Lorentzian amplitude (S_0/ξ^2) as obtained from fits of the Cu_I static structure factor to a single 2D Lorentzian. Different open symbols denote different experimental configurations. In (b), they are scaled to match in the overlapping temperature range. Solid squares in (a) are Monte Carlo results,^{6,39,64} and the solid lines are theoretical predictions from the QNL σ M with $J = 130\text{meV}$.

describe our data equally well.

B Cu_{II} system

The Cu_{II} two-axis cross section is given by

$$I(q_{2D}) = \int_{-\infty}^{E_i} d\omega S(\mathbf{Q}, \omega) \quad (19)$$

$$\sim [(2 + \sin^2(\phi))S^T(q_{2D}) + (1 + \cos^2(\phi))S^L(q_{2D})],$$

where $q_{2D} \equiv \frac{2\pi}{a} \sqrt{(H - \frac{1}{2})^2 + (K - \frac{1}{2})^2}$, and S^T and S^L are the transverse and longitudinal components of the static fluctuations. S^L diverges at the Ising ordering temperature $T_{N,II}$. The particular geometric factors result from the fact that the Cu_{II} easy-axis lies within the copper oxide layers and that there exist two types of domains that are equally probable. This gives an almost 3 to 1 ratio of transverse to longitudinal components when L is

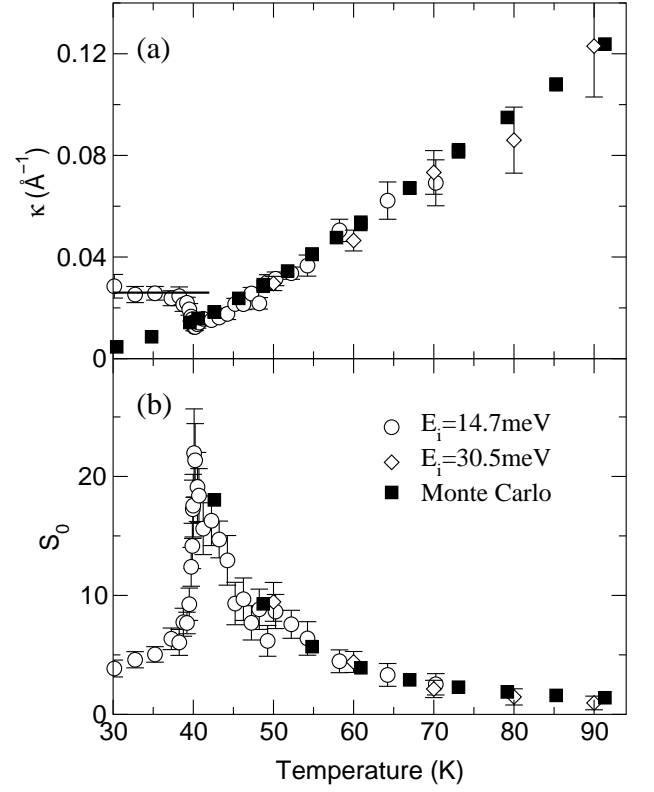


FIG. 17: (a) Inverse magnetic correlation length and (b) static structure factor peak amplitude S_0 as obtained from fits to a single 2D Lorentzian. Different open symbols denote different experimental configurations. In (b), they are scaled to match in the overlapping temperature range. Solid squares are Monte Carlo results,^{6,39,64} and the solid line at $T < 40\text{K}$ in (a) is $\kappa = 0.026\text{\AA}^{-1}$ as described in the text.

small, making it difficult to observe longitudinal fluctuations. In K_2NiF_4 , where the easy-axis is perpendicular to the NiF_2 plane, this ratio is close to 1:1, enabling one to observe readily the longitudinal (Ising) component of the static structure factor.³⁶

Our experiment was carried out with $E_i = 14.7\text{meV}$ and with collimations $20^\circ\text{-}40^\circ\text{-}S\text{-}40^\circ$. Representative scans are shown in Fig. 15(b). At higher temperatures, we used $E_i = 30.5\text{meV}$ in order to ensure that the energy integration is done properly, since the characteristic energy scale becomes large at these temperatures. We could not distinguish the longitudinal component from the transverse component; therefore, the solid lines in Fig. 15(b) are results of fits to a single 2D Lorentzian, Eq. (17), convoluted with the experimental resolution. The so-obtained correlation lengths versus temperature are plotted in Fig. 17(a). Also shown are Monte Carlo results for the $S = 1/2$ nearest-neighbor SLQHA.^{6,39,64} At temperatures well above $T_{N,II}$ the spin system is effectively isotropic, and the correlation length agrees very well with

the numerical result. However, even at lower temperatures the agreement is quite good, since the transverse term in the cross section is 3 times larger than the longitudinal term. In addition, Ising criticality has a very small critical temperature range. As the temperature is lowered, the crossover from the 2D Heisenberg to the 2D Ising symmetry presumably occurs very close to the transition temperature, $T_{N,II}$, and hence isotropic behavior is observed for $T \gtrsim T_{N,II}$. We also show the static structure factor peak amplitude S_0 in Fig. 17(b) along with the Monte Carlo results from Ref. 66. Similar to the inverse correlation length data, the agreement is quite good for all $T \gtrsim T_{N,II}$.

At temperatures below $T_{N,II}$, the inverse correlation length shows a saturation around 0.025\AA^{-1} . In their study of the 2D antiferromagnets, Birgeneau *et al.*⁶⁷ showed that the transverse susceptibility dominates below the Néel temperature and it can be described via spin wave theory. In the presence of an Ising anisotropy, α , a typical spin wave dispersion is given as $\omega_q \propto \sqrt{8J^2Z_g^2\alpha + v^2q^2/2}$ and the spin wave intensity is proportional to $1/\omega_q$, where v is the spin wave velocity, $2S\sqrt{2}Z_cJa$. For $\omega/T \ll 1$, the population factor is reduced to ω_q^{-1} . Thus the neutron scattering intensity of the wave vector dependent susceptibility is

$$I \sim \omega_q^{-2} \sim \frac{1}{Z_c^2 J^2 a^2 q^2 + 8J^2 Z_g^2 \alpha} \sim \frac{1}{q^2 + \kappa_\perp^2}, \quad (20)$$

which is a Lorentzian with a finite width, $\kappa_\perp \equiv \frac{2Z_g}{aZ_c} \sqrt{2\alpha}$. By substituting $\alpha_{II}^{eff} \approx 0.01$ for the α , we obtain $\kappa_\perp \approx 0.026\text{\AA}^{-1}$. This value, indicated as a solid line in the figure, agrees remarkably well with the experimental results.

In Fig. 18, the correlation length data for $T > 43\text{K}$ are plotted as a function of inverse temperature on a semi-log scale. Also plotted are the correlation length data of $\text{Sr}_2\text{CuO}_2\text{Cl}_2$ taken from Ref. 7. These neutron scattering data are compared with various theoretical predictions. The RC expression for the correlation length is plotted as a dot-dashed line. Quantum Monte Carlo results and high temperature series expansion results⁶⁸ are shown as solid and dotted lines, respectively. In a recent theoretical study, Cuccoli *et al.*⁶⁹ treated quantum fluctuations in a self-consistent Gaussian approximation, separately from the classical contribution. This purely-quantum self-consistent harmonic approximation (PQSCHA) result is plotted as a dashed line in Fig. 18. The combined experimental data span almost two orders of magnitude in correlation length and show quantitative agreement with the Monte Carlo results without any adjustable parameters. At high temperatures, $\xi/a \lesssim 10$, both the series expansion and the PQSCHA, which corresponds to classical scaling, agree with the experimental data within error bars. The surprisingly good agreement between the neutron scattering data and the renormalized classical prediction even up to a very high temper-

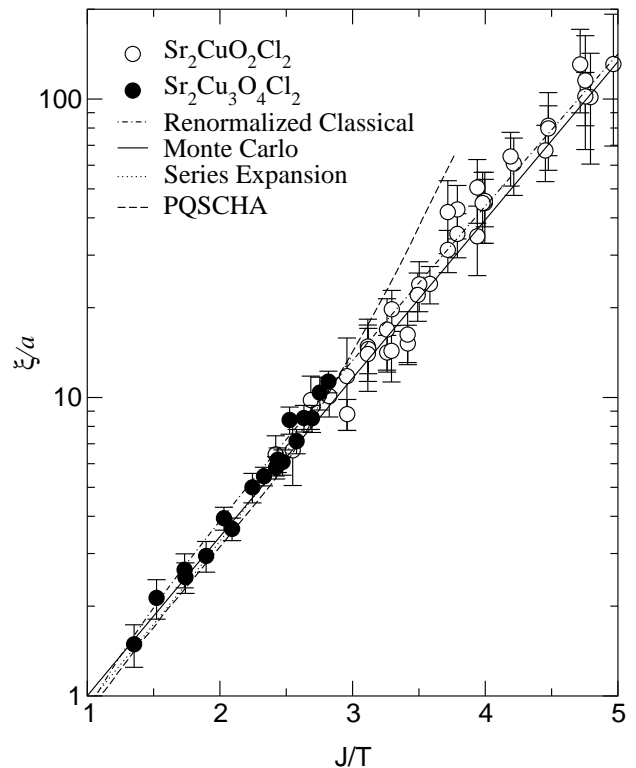


FIG. 18: The logarithm of the reduced magnetic correlation length ξ/a versus J/T . The open and filled circles are the data for $\text{Sr}_2\text{CuO}_2\text{Cl}_2$ (Ref. 7) and $\text{Sr}_2\text{Cu}_3\text{O}_4\text{Cl}_2$ (Cu_{II}), respectively. The RC prediction of the QNL σ M is plotted in dot-dashed line. Interpolated quantum Monte Carlo results^{6,39,64} and high temperature series expansion results⁶⁸ are shown in solid and dotted line, respectively. Cuccoli *et al.*'s PQSCHA result⁶⁹ is plotted as a dashed line.

ature turns out to be a fortuitous one. Beard *et al.*⁶ pointed out that the renormalized classical scaling sets in only at large correlation lengths so that the temperature range probed by the neutron scattering experiment ($T \gtrsim 0.2J$) is not low enough to see this asymptotic scaling behavior. However, the deviation is smaller than the experimental errors, making it difficult to discern any discrepancies from the neutron scattering experiment.

There are two other recent neutron scattering studies on the magnetic correlation length of the $S = 1/2$ SLQHA. Birgeneau *et al.*⁸ extended previous work on La_2CuO_4 to higher temperature and showed that the data are well-described by the Monte Carlo, the PQSCHA, and series expansion results within the experimental uncertainties. They also showed that there is no evidence for a crossover from renormalized classical to quantum critical behavior, at least from the correlation length data. Rønnow *et al.*⁷⁰ also have carried out a study of the correlation length in the monoclinic planar antiferromagnet copper formate tetra-deuterate

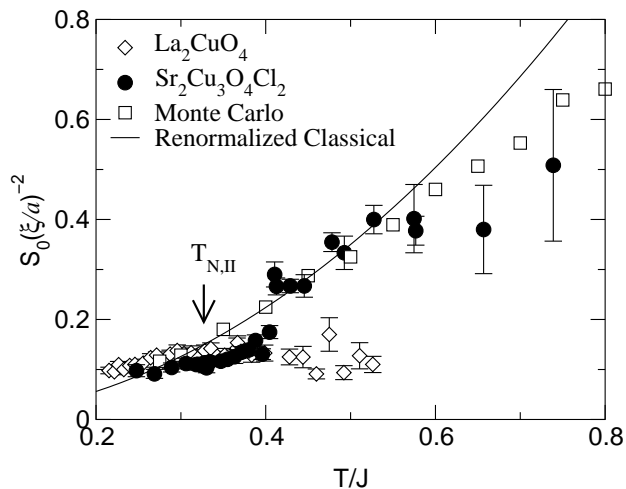


FIG. 19: The Lorentzian amplitude of the structure factor, $S_0(\xi/a)^{-2}$, is plotted as a function of T/J . The open and filled circles are the data for La_2CuO_4 (Ref. 8) and $\text{Sr}_2\text{Cu}_3\text{O}_4\text{Cl}_2$ (Cu_{II}), respectively. The RC prediction of the QNL σ M is plotted as a solid line. Our quantum Monte Carlo results are also shown in open squares.

(CFTD). They obtained essentially similar results to those shown here for the Cu_{II} system, agreeing with the Monte Carlo data up to a very high temperature ($T \approx 1.25J$). They were able to extend their measurement to such a high temperature by employing a special technique involving filtering out the elastic part of the signal, thus reducing the incoherent background. However, the analysis depends sensitively on the theoretical model, especially on the scaling of the characteristic energy scale $\Gamma_{\mathbf{q}=0}$, which still needs further investigation. Besides, its low-symmetry crystal structure and relatively large Dzialoshinsky-Moriya interaction make CFTD a less ideal $S = 1/2$ SLQHA than $\text{Sr}_2\text{Cu}_3\text{O}_4\text{Cl}_2$ (Cu_{II}). In fact, the combined $\text{Sr}_2\text{CuO}_2\text{Cl}_2$ - $\text{Sr}_2\text{Cu}_3\text{O}_4\text{Cl}_2$ (Cu_{II}) system forms an ideal model $S = 1/2$ SLQHA over a large temperature range $0.2 \lesssim T/J \lesssim 0.75$.

In Fig. 19, the Lorentzian amplitude of the structure factor, $S_0(\xi/a)^{-2}$, is plotted as a function of T/J . Our data and the La_2CuO_4 data of Birgeneau *et al.*⁸ are scaled to match the Monte Carlo results, which are plotted in absolute units without any free parameter. The RC prediction is also plotted as a solid line: $\frac{S_0}{\xi^2} = A2\pi M_S^2 \left(\frac{T}{2\pi\rho_S}\right)^2$, with $A_{S=1/2} = 3.2$ from the series expansion study.⁷¹ The first thing to note in our data is the disappearance of the divergence at $T_{N,II}$, which implies that the divergence in S_0 is absorbed by the ξ^2 term, or equivalently $\eta = 0$, as predicted for the 2D Heisenberg model. On the other hand, the critical exponent η for the 2D Ising model is exactly known to be $\eta = 1/4$; thus $S_0\xi^{-2}$ should show a weak divergence of $\xi^{-1/4} = (T_N - T)^{-1/4}$, which is not observed. This is

not surprising, since the finite Q -resolution prevents us from observing even the strong divergence of ξ in the first place.

What is surprising, however, is the discrepancy observed at high temperatures between the two experimental sets of data. Unlike La_2CuO_4 , which shows constant $S_0\xi^{-2}$ over the observed temperature range, the Cu_{II} system shows some temperature dependence. Specifically, $S_0\xi^{-2}$ follows the Monte Carlo data closely for $T \gtrsim 0.4J$ and deviates significantly from the RC prediction at high temperatures. $S_0\xi^{-2}$ for $\text{Sr}_2\text{CuO}_2\text{Cl}_2$ shows behavior similar to that of La_2CuO_4 , while CFTD shows behavior similar to that of $\text{Sr}_2\text{Cu}_3\text{O}_4\text{Cl}_2$. Considering that the CFTD also has rather small exchange coupling of $\sim 6.3\text{meV}$,⁷⁰ one can speculate that this discrepancy may be due to high energy fluctuations at high temperatures, which are not integrated in the experiments on systems with a large exchange interaction, such as La_2CuO_4 . An experimental study on dynamic critical behavior of the 2DQHA is necessary to address this problem further.

Recently, in their study of the $S = 5/2$ SLQHA, Rb_2MnF_4 , Leheny *et al.*⁷² showed that the amplitude $S_0\xi^{-2}$ crosses over from constant behavior at high temperature to the $\sim T^2$ behavior at low temperature. The crossover temperature was estimated to be around $\sim 7.4J$, which would correspond to $\sim 0.6J$ for the $S = 1/2$ case, after the temperature scaling of $S(S+1)$ is taken into account. One might be able to regard the high temperature data for $T/J \geq 0.6$ of $S_0\xi^{-2}$ as constant, thus showing similar crossover behavior, although it is difficult to make any strong statement with the current data.

VI. DISCUSSION

From our study, we have been able to determine two very important superexchange interactions: one is the “edge-sharing” $\text{Cu}_I\text{-O-Cu}_{II}$ exchange interaction, and the other is the $\text{Cu}_{II}\text{-Cu}_{II}$ interaction, which corresponds to the second nearest neighbor interaction in the Cu_I square lattice. First, we estimate the isotropic $\text{Cu}_I\text{-Cu}_{II}$ interaction as $J_{I-II} \approx -10\text{meV}$. This edge sharing superexchange interaction is crucial in understanding spin ladder materials, SrCu_2O_3 and $\text{Sr}_{14}\text{Cu}_{24}\text{O}_{41}$, as well as other 1D spin systems, such as SrCuO_2 ($S = 1/2$ zigzag chain) and CaCu_2O_3 (buckled ladder). It has been assumed that the edge sharing interactions, which happen to be frustrated in all these materials, are small, and that they therefore can be ignored in data analysis. However, as we have seen in $\text{Sr}_2\text{Cu}_3\text{O}_4\text{Cl}_2$, quantum effects may be important in understanding the low temperature properties of these systems.

The second nearest neighbor interaction in the copper oxide plane of the high temperature superconductors has the same superexchange path as the $\text{Cu}_{II}\text{-Cu}_{II}$ interaction; namely, the Cu-O-O-Cu path. Of course, the $\text{Cu}_{II}\text{-Cu}_{II}$ interaction has additional contributions from

the path Cu–O–Cu–O–Cu; however, one would expect this contribution to be small in magnitude; it should also be ferromagnetic. Thus, we can assume that the second nearest neighbor coupling in the copper oxide plane must be close to the J_{II} value: ~ 10 meV. This value is used to fit the ARPES data in the framework of the $t-t'-t''-J$ model by Kim *et al.*,¹⁰ which shows good agreement.

One expects interesting physics to arise from doping this system with either charge carriers or non-magnetic impurities. One difficulty of studying doped $\text{Sr}_2\text{Cu}_3\text{O}_4\text{Cl}_2$ is that it is extremely difficult to dope this system with any impurities. Many attempts to dope this system with impurities such as Zn, Mg, K, Y, etc. have failed. In fact, there are only two successfully doped copper oxy-hallides: $\text{Sr}_2\text{CuO}_2\text{F}_{2+\delta}$ by Al-Mamouri *et al.*⁷³ and $(\text{Ca},\text{Na})_2\text{CuO}_2\text{Cl}_2$ by Hiroi *et al.*⁷⁴ Both compounds are superconducting and are synthesized at high-pressure.

In his study of a frustrated vector antiferromagnet, where the next nearest neighbor coupling is much greater than the nearest neighbor coupling, Henley²⁷ has shown that the disorder introduced by dilution favors *anti-collinear* ordering. Since quantum fluctuations prefer a collinearly ordered ground state, these two types of disorder compete with each other and produce a rich phase diagram as a function of temperature and dilution. However, diluted $\text{Sr}_2\text{Cu}_3\text{O}_4\text{Cl}_2$ is a little different in that the relevant coupling ratio (J_{I-II}/J_{II}) is not small, so that the simple perturbation expansion used by Henley is no longer applicable. Nevertheless we expect a dramatic change in the ground state of diluted $\text{Sr}_2\text{Cu}_3\text{O}_4\text{Cl}_2$; for example, a helical order, a spin glass, or even a disordered ground state might occur as a result of dilution.

VII. CONCLUSIONS

We have presented results from our neutron scattering experiments on $\text{Sr}_2\text{Cu}_3\text{O}_4\text{Cl}_2$, and discussed its magnetic properties as well as the novel quantum phenomena associated with *order from disorder*. In what follows, we briefly summarize our main results.

(1) Our elastic neutron diffraction data confirm the magnetic structure obtained from a previous analysis²² of static properties in a magnetic field.

(2) We show that $\text{Sr}_2\text{Cu}_3\text{O}_4\text{Cl}_2$ is a unique system having two independent phase transitions. By analyzing the intensities of the magnetic Bragg reflections we obtain the critical exponents for the order parameter for the Cu_I transition at $T_{N,I} = 386(2)\text{K}$ $\beta_I = 0.28(3)$ and for the Cu_{II} transition at $T_{N,II} = 39.6(4)\text{K}$ $\beta_{II} = 0.13(1)$. The Cu_I transition is thought to be that of a 3D XY model, whereas the Cu_{II} transition is identified as a 2D Ising transition.

(3) The dramatic variation in the mode energies as the Cu_{II} subsystem orders is very clear evidence of quantum fluctuations because on the mean field level the interac-

tion between these subsystems is frustrated. Some modes (i. e. ω_3) would have zero energy in the absence of quantum fluctuations. Other modes (i. e. ω_2 and ω_4) show remarkable effects of quantum fluctuations. In all cases, these dramatic shifts are in quantitative agreement with theoretical calculations.

(4) Our measurement of the spin-wave dispersion allows precise determination of several exchange interactions, including the interplanar Cu_I - Cu_I interaction ($J_{I,3D} = 0.14(2)$ meV), the in-plane Cu_{II} - Cu_{II} interaction ($J_{II} = 10.5(5)$ meV), and the in-plane Cu_I - Cu_{II} interaction ($|J_{I-II}| = 10(2)$ meV).

(5) We have made precise tests of spin-wave interactions at the zone boundary which support recent theoretical calculations. This test is particularly convincing for this spin 1/2 system, where these effects are too large to be attributed to further-than-nearest neighbor interactions.

(6) The instantaneous spin-spin correlation length, ξ , of $S = 1/2$ SLQHA over a wide temperature range has also been obtained from our neutron scattering experiments. Our measured values of ξ are in good agreement with recent calculations based on the quantum nonlinear σ model and on quantum Monte Carlo simulations.

ACKNOWLEDGMENTS

This work was supported by the US-Israel Binational Science Foundation (at Tel Aviv, MIT and Penn), by the NSF grant No. DMR97-04532 and by the MRSEC Program of the NSF under award No. DMR98-08941 (at MIT), under contract No. DE-AC02-98CH10886, Division of Material Science, U. S. Department of Energy (at BNL), and by the NSF under agreement No. DMR-9423101 (at NIST).

REFERENCES

- ^a Present address: Department of Physics, Brookhaven National Laboratory, Upton, New York 11973.
- ^b Also at: Department of Physics, University of Toronto, Toronto, Ontario M5S 1A7, Canada.
- ^c Present address: Department of Applied Physics and Stanford Synchrotron Radiation Laboratory, Stanford University, Stanford, California 94305.
- ^d Present address: Center for Neutron Research, National Institute of Standards and Technology, Gaithersburg, Maryland 20899.
- ^e Present address: Department of Physics, University of Connecticut, Storrs, Connecticut 06269.
- ¹ G. Horwitz and H. B. Callen, Phys. Rev. **124**, 1757 (1961); V. G. Vaks, A. I. Larkin, and S. A. Pikin, Sov. Phys.-JETP **26**, 188 (1968); A. B. Harris, Phys. Rev. Lett. **21**, 602 (1968); R. B. Stinchcombe, G. Horwitz, F. Englert, and R. Brout, Phys. Rev. **130**, 155 (1963).

- ² F. D. M. Haldane, Phys. Lett. **93A**, 464 (1983).
- ³ S. Chakravarty, B. I. Halperin, and D. R. Nelson, Phys. Rev. B **39**, 2344 (1989).
- ⁴ E. F. Shender, Sov. Phys. JETP **56**, 178 (1982).
- ⁵ Y. J. Kim, R. J. Birgeneau, F. C. Chou, M. Greven, M. A. Kastner, Y. S. Lee, A. Aharony, O. Entin-Wohlman, I. Ya. Korenblit, A. B. Harris, R. W. Erwin, and G. Shirane, Phys. Rev. Lett. **83**, 852 (1999).
- ⁶ B. B. Beard, R. J. Birgeneau, M. Greven, and U. J. Wiese, Phys. Rev. Lett. **80**, 1742 (1998).
- ⁷ M. Greven, R. J. Birgeneau, Y. Endoh, M. A. Kastner, M. Matsuda, and G. Shirane, Z. Phys. B **96**, 465 (1995).
- ⁸ R. J. Birgeneau, M. Greven, M. A. Kastner, Y. S. Lee, B. O. Wells, Y. Endoh, K. Yamada, and G. Shirane, Phys. Rev. B **59**, 13788 (1999).
- ⁹ B. O. Wells, Z. X. Shen, A. Matsuura, D. M. King, M. A. Kastner, M. Greven, and R. J. Birgeneau, Phys. Rev. Lett. **74**, 964 (1995).
- ¹⁰ C. Kim, P. J. White, Z.-X. Shen, T. Tohyama, Y. Shibata, S. Maekawa, B. O. Wells, Y. J. Kim, R. J. Birgeneau, and M. A. Kastner, Phys. Rev. Lett. **80**, 4245 (1998).
- ¹¹ B. Grande and H. Müller-Buschbaum, Z. Naturforsch. **B31**, 405 (1976).
- ¹² H. Müller-Buschbaum, Angew. Chem. Int. Ed. Engl. **16**, 674 (1977).
- ¹³ S. Noro, H. Suzuki, and T. Yamadaya, Solid State Comm. **76**, 711 (1990).
- ¹⁴ K. Yamada, N. Suzuki, and J. Akimitsu, Physica B **213-214**, 191 (1995).
- ¹⁵ N. Adachi, T. Hamamoto, G. Kodo, M. Hase, Y. Sasago, K. Uchinokura, S. Noro, and T. Yamadaya, Physica B **76**, 711 (1990).
- ¹⁶ H. Ohta, M. Sumikawa, M. Motokawa, S. Noro, and T. Yamadaya, J. Phys. Soc. Jpn **64**, 1759 (1995).
- ¹⁷ M. S. Golden, H. C. Schmelz, M. Knupfer, S. Haffner, G. Krabbes, J. Fink, V. Y. Yushankhai, H. Rosner, R. Hayn, A. Müller, and G. Reichardt, Phys. Rev. Lett. **78**, 4107 (1997).
- ¹⁸ H. C. Schmelz, M. S. Golden, S. Haffner, M. Knupfer, G. Krabbes, J. Fink, H. Rosner, R. Hayn, H. Eschrig, A. Müller, C. Jung, and G. Reichardt, Phys. Rev. B **57**, 10936 (1998).
- ¹⁹ S. Haffner, R. Neudert, M. Kielwein, M. Knupfer, M. S. Golden, K. Ruck, G. Krabbes, J. Fink, H. Rosner, R. Hayn, H. Eisaki, S. Uchida, Z. Hu, M. Donke, and G. Kaindl, Phys. Rev. B **57**, 3672 (1998).
- ²⁰ F. C. Chou, A. Aharony, R. J. Birgeneau, O. Entin-Wohlman, M. Greven, A. B. Harris, M. A. Kastner, Y. J. Kim, D. S. Kleinberg, Y. S. Lee, and Q. Zhu, Phys. Rev. Lett. **78**, 535 (1997).
- ²¹ T. Ito, H. Yamaguchi, and K. Oka, Phys. Rev. B **55**, R684 (1997).
- ²² M. A. Kastner, A. Aharony, R. J. Birgeneau, F. C. Chou, O. Entin-Wohlman, M. Greven, A. B. Harris, Y. J. Kim, Y. S. Lee, M. E. Parks, and Q. Zhu, Phys. Rev. B **59**, 14702 (1999).
- ²³ T. Brückel, B. Dorner, A. G. Gukasov, V. P. Plakhty, W. Prandl, E. F. Shender, and O. P. Smirnov, Z. Phys. B **72**, 477 (1988).
- ²⁴ A. G. Gukasov, T. Brückel, B. Dorner, V. P. Plakhty, W. Prandl, E. F. Shender, and O. P. Smirnov, Europhys. Lett. **7**, 83 (1988).
- ²⁵ T. Brückel, B. Dorner, A. Gukasov, and V. P. Plakhty, Phys. Lett. A **162**, 357 (1992).
- ²⁶ J. Villain, R. Bidaux, J. P. Carton, and R. Conte, J. Phys. (Paris) **41**, 1263 (1980).
- ²⁷ C. L. Henley, Phys. Rev. Lett. **62**, 2056 (1989).
- ²⁸ P. Chandra, P. Coleman, and A. I. Larkin, Phys. Rev. Lett. **64**, 88 (1990).
- ²⁹ E. Rastelli, S. Sedazzari, and A. Tassi, J. Phys. Condens. Matter **2**, 8935 (1990).
- ³⁰ T. Yildirim, A. B. Harris, and E. F. Shender, Phys. Rev. B **53**, 6455 (1996).
- ³¹ T. Yildirim, A. B. Harris, and E. F. Shender, Phys. Rev. B **58**, 3144 (1998).
- ³² E. F. Shender and P. C. W. Holdsworth, in *Fluctuations and order : the new synthesis*, edited by M. Millonas (Springer, New York, 1996), pp. 259–279.
- ³³ S. W. Lovesey, *Theory of Neutron Scattering from Condensed Matter* (Oxford University Press, Oxford, 1984).
- ³⁴ G. L. Squires, *Introduction to the theory of thermal neutron scattering* (Cambridge University Press, Cambridge, 1978).
- ³⁵ P. J. Brown, in *International tables for crystallography, v. C. Mathematical, physical and chemical tables*, edited by A. Wilson (D. Reidel Pub. Co., Dordrecht, Holland, 1995), pp. 391–399.
- ³⁶ R. J. Birgeneau, J. Skalyo, Jr., and G. Shirane, Phys. Rev. B **3**, 1736 (1971).
- ³⁷ B. J. Suh, F. Borsa, L. L. Miller, M. Corti, D. C. Johnston, and D. R. Torgeson, Phys. Rev. Lett. **75**, 2212 (1995).
- ³⁸ B. Keimer, A. Aharony, A. Auerbach, R. J. Birgeneau, A. Cassanho, Y. Endoh, R. W. Erwin, M. A. Kastner, and G. Shirane, Phys. Rev. B **45**, 7430 (1992).
- ³⁹ J. K. Kim and M. Troyer, Phys. Rev. Lett. **80**, 2705 (1998).
- ⁴⁰ T. Yildirim, A. B. Harris, O. Entin-Wohlman, and A. Aharony, Phys. Rev. Lett. **72**, 3710 (1994).
- ⁴¹ D. Vaknin, S. K. Sinha, C. Stassis, L. L. Miller, and D. C. Johnston, Phys. Rev. B **41**, 1926 (1990).
- ⁴² S. Shamoto, M. Sato, J. M. Tranquada, B. J. Sternlieb, and G. Shirane, Phys. Rev. B **48**, 13817 (1993).
- ⁴³ E. Manousakis, Rev. Mod. Phys. **63**, 1 (1991).
- ⁴⁴ B. Keimer, Ph.D. thesis, Massachusetts Institute of Technology, 1991.
- ⁴⁵ S. Bramwell and P. Holdsworth, J. Phys. Condens. Matter **5**, L53 (1993).
- ⁴⁶ T. Thio and A. Aharony, Phys. Rev. Lett. **73**, 894 (1994).
- ⁴⁷ G. Shirane, Y. Endoh, R. J. Birgeneau, M. A. Kastner, Y. Hidaka, M. Oda, M. Suzuki, and T. Murakami, Phys. Rev. Lett. **59**, 1613 (1987).

- ⁴⁸ K. Katsumata, M. Hagiwara, Z. Honda, J. Satooka, A. Aharony, R. J. Birgeneau, F. C. Chou, O. Entin-Wohlman, A. B. Harris, M. A. Kastner, Y. J. Kim, and Y. S. Lee, cond-mat/0008009.
- ⁴⁹ A. B. Harris, A. Aharony, O. Entin-Wohlman, I. Ya. Korenblit, R. J. Birgeneau, and Y. J. Kim, unpublished.
- ⁵⁰ T. Barnes, K. J. Cappon, E. Dagotto, D. Kotchan, and E. S. Swanson, Phys. Rev. B **40**, 8945 (1989).
- ⁵¹ W. Zheng, J. Oitmaa, and C. J. Hamer, Phys. Rev. B **43**, 8321 (1991).
- ⁵² R. R. P. Singh and M. P. Gelfand, Phys. Rev. B **52**, R15695 (1995).
- ⁵³ T. Oguchi, Phys. Rev. **117**, 117 (1960).
- ⁵⁴ R. R. P. Singh, Phys. Rev. B **39**, 9760 (1989).
- ⁵⁵ J. Igarashi, Phys. Rev. B **46**, 10763 (1992).
- ⁵⁶ F. Keffer, in *Handbuch der Physik Vol. XVIII/2 - Ferromagnetism*, edited by H. P. J. Wijn (Springer-Verlag, Berlin, 1966), pp. 1–273.
- ⁵⁷ T. Yildirim, A. B. Harris, O. Entin-Wohlman, and A. Aharony, Phys. Rev. Lett. **73**, 2919 (1994).
- ⁵⁸ C. M. Canali, S. M. Girvin, and M. Wallin, Phys. Rev. B **45**, 10131 (1992).
- ⁵⁹ S. Winterfeldt and D. Ihle, Phys. Rev. B **56**, 5535 (1997).
- ⁶⁰ O. F. Syljuåsen and H. M. Rønnow, J. Phys. Condens. Matter **12**, L405 (2000).
- ⁶¹ S. M. Hayden, G. Aeppli, R. Osborn, A. D. Taylor, T. G. Perring, S. W. Cheong, and Z. Fisk, Phys. Rev. Lett. **67**, 3622 (1991).
- ⁶² Y. Tokura, S. Koshihara, T. Arima, H. Takagi, S. Ishibashi, T. Ido, and S. Uchida, Phys. Rev. B **41**, 11657 (1990).
- ⁶³ D. Bloch, J. Phys. Chem. Solids **27**, 881 (1966).
- ⁶⁴ M. Greven, R. J. Birgeneau, and U.-J. Wiese, Phys. Rev. Lett. **77**, 1865 (1996).
- ⁶⁵ P. Hasenfratz and F. Niedermayer, Phys. Lett. B **268**, 231 (1991).
- ⁶⁶ Y. J. Kim, Ph.D. thesis, Harvard University, 1999.
- ⁶⁷ R. J. Birgeneau, J. Als-Nielsen, and G. Shirane, Phys. Rev. B **16**, 280 (1977).
- ⁶⁸ N. Elstner, Int. J. Mod. Phys. B **11**, 1753 (1997).
- ⁶⁹ A. Cuccoli, V. Tognetti, R. Vaia, and P. Verrucchi, Phys. Rev. B **56**, 14456 (1997).
- ⁷⁰ H. M. Rønnow, D. F. McMorrow, and A. Harrison, Phys. Rev. Lett. **82**, 3152 (1999).
- ⁷¹ N. Elstner, A. Sokol, R. R. P. Singh, M. Greven, and R. J. Birgeneau, Phys. Rev. Lett. **75**, 938 (1995).
- ⁷² R. L. Leheny, R. J. Christianson, R. J. Birgeneau, and R. W. Erwin, Phys. Rev. Lett. **82**, 418 (1999).
- ⁷³ M. Al-Mamouri, P. P. Edwards, C. Greaves, and M. Slaski, Nature **369**, 382 (1994).
- ⁷⁴ Z. Hiroi, N. Kobayashi, and M. Takano, Nature **371**, 139 (1994).